Sulfur, selenium and tellurium fractionation during magma crystallization and degassing: constraints from Southwest Indian Ocean volcanism (La Réunion Island and Mayotte Fani Maoré eruption)

Ivan Vlastélic, Jean-Luc Piro, Vincent Famin, Carole Berthod, Patrick Bachèlery, Thomas Rouyer, Andrea Dimuro

Sulfur, selenium and tellurium fractionation during magma crystallization and degassing: constraints from Southwest Indian Ocean volcanism (La Réunion Island and Mayotte Fani Maoré eruption)

Ms in preparation October 20, 2024 to be submitted to Chemical Geology

I. Vlastélic[1,2,*], J.-L. Piro[1], V. Famin[2,3], C. Berthod[2], P. Bachèlery[1], T. Rouyer[1], A. Di Muro[4]

1 Université Clermont Auvergne, CNRS, IRD, OPGC, Laboratoire Magmas et Volcans, F-63000 Clermont-Ferrand, France

2 Université Paris-Cité, Institut de physique du globe de Paris, CNRS, UMR 7154, F-75005 Paris, France

3 Université de La Réunion, Laboratoire GéoSciences Réunion, F-97744 Saint-Denis, France

4 Laboratoire de Géologie de Lyon Terre - Planètes – Environnement, Observatoire de Lyon, UAR 3721 COMET

• Corresponding author

Abstract

Selenium (Se) and tellurium (Te) are oxygen group elements that share chemical properties with sulfur, but also show subtle differences that are useful to constrain magma genesis and source. Using high-precision isotope dilution measurements, this study characterizes the behavior of Se and Te, relatively to S, during the degassing and crystallization of cogenetic magmas from the southwest Indian Ocean. The study of subaerial and submarine lavas from La Réunion Island first shows that, unlike S and Te, Se is not significantly lost during the rapid, final ascent of less differentiated magmas (MgO > 6wt%). This is because Se is retained as selenide in primary melts despite relatively oxidized conditions. Conversely, selenium degassing occurs during magma crystallization below 6 wt% MgO, at a similar rate as sulfur, yielding small S/Se fractionation in the residual magma. Sulfide fractionation, which begins between 5 and 4 wt% MgO, has minor effect on Se compared to Cu. Tellurium is extensively outgassed from La Réunion subaerial lavas but shows a very specific behavior in submarine lavas where it is retained and even accumulate near 6 wt% MgO. The very different behaviors of Se and Te during magma degassing yields extremely large Se/Te variations between subaerial (up to 225) and submarine (down to 1) lavas from La Réunion. The Fani Maoré eruption that occurred between 2018 and 2021 offshore the island of Mayotte (Comoros Archipelago) also provided the opportunity to study chalcogens degassing during the emplacement of submarine lavas. The study of a pillow lava showing a radial textural zonation typical of degassing-crystallization during cooling reveals that S, Se and other moderately volatile elements (Mo, W, Cs) are the most depleted at intermediate depth within the pillow where pipe vesicles occur, suggesting these elements escape with major volatiles. Conversely, Te is depleted in the whole interior of the pillow, suggesting Te escapes through other means. Assessment of pillow degassing during emplacement yields a 6.5% loss of the initial S content, 7.2% for Te, but only 1.6% for Se confirming the lower volatility of Se during lava emplacement. Chalcogens degassing is accompanied with significant loss of W (8.9%), Mo (5.1%) and Cs (5.1%) from Fani Maoré lavas. Based on these values, the 6.5 km^3 Fani Maoré eruption released 1.1 – 1.5 x 10^6 tons of S, 2300 – 2700 tons of Mo, 970 – 1130 tons of W, 194 – 339 tons of Cs, 13.3 – 16 tons of Se and 4.5 – 11.8 tons of Te during emplacement. The unusually elevated S/Se ratios (16929 — 22130) of Fani Maoré lavas requires a mantle source extensively fertilized by sulfide melts, whereas the reconstructed S – Se – Te composition of

La Réunion plume source is consistent with the preservation of chondritic S/Se and Se/Te ratios.

Keywords : selenium, tellurium, magma degassing, magma differentiation, La Réunion, Mayotte, Fani Maoré eruption

1. Introduction

Selenium (Se) and tellurium (Te) are group 16 elements sharing chemical and physical properties with the element sulfur. In particular S^{2-} , Se^{2-} and Te^{2-} have very similar ionic radii (Shannon et al., 1976) allowing extensive substitution in reducing conditions. These elements are the object of a growing interest because Se and Te are useful elements to constrain models of Earth accretion and differentiation (Wang and Becker, 2013), upper mantle processes such partial melting and refertilization of the lithosphere (Lorand and Allard, 2010; König et al., 2012), while Se plays an important role in biogeochemical cycle (Sharma et al., 2015). Selenium and tellurium are highly volatile elements but also tend to substitute for sulfur in immiscible sulfide liquids. This dual nature led to different views regarding the fate Se and Te during magma genesis an eruption. On the one hand, studies of mantle rocks, ultramafic cumulates and lavas show that Se and Te are trapped in dense sulfides that accumulate in the deep roots of volcanoes (Hertogen et al., 1980; Lissner et al., 2014; Collins et al., 2012; Yierpan et al., 2019). On the other hand, studies of more-or-less degassed lavas (Yierpan et al., 2021) and volcanic gas products (Greenland and Aruscavage; 1986; Zelenski et al., 2021; Rosca et al., 2021) show that Se and Te extensively partition into the vapor phase and are delivered to the outer layers of the Earth. At the heart of this debate is the timing of sulfide saturation relative to magma degassing, and the degree to which Se and Te partition into sulfide melts relative to the gas phase. Edmonds et al. (2018) suggest that sulfide saturation control the metal signature of volcanic gas, and its variations in arc and hotspot settings. Conversely, Zelenski et al. (2021) suggest that the trace element budget of volcanic gas is mainly determined by the near-surface partitioning of elements between gas and silicate melt.

This paper investigates the S – Se – Te signature of La Réunion hotspot magmatic system to constrain the nature of the hotspot source, and the role of sulfide saturation versus degassing on the composition of the erupted lavas. Our approach is based on the study of cogenetic rocks including plutonic rocks and lavas showing a wide range of degassing (submarine and subaerial) and crystallization (basalt to trachyte) extents, as well as contrasted cooling rates (lava flow and glassy tephra). We also compare the S-Se-Te signature of the low-pressure Réunion magmas to the signature of the high-pressure sulfide saturated magmas that were emitted during the 2018-2021 Fani Maoré eruption offshore the Mayotte Island (Berthod et al., 2021, 2022). The results show that the residual abundances of S, Se and Te in lavas are

dominantly controlled by degassing processes, unlike less volatile Cu, which records the deeper processes of sulfide saturation.

2. Geological setting

The island of La Réunion (Indian Ocean) is the present location of the hotspot that created the Deccan traps ca. 66 Ma ago (Fig. 1a). The oldest submarine activity is dated at 3.8 Ma (Smietana, 2011), but the edifice most likely started to grow ca. 5 Myr ago (Bonneville et., 1988). The emergent part of the island comprises a quiescent volcano (Piton des Neiges) in the NW and a basaltic shield volcano (Piton de la Fournaise) in the SE (Fig. 1b). Piton des Neiges produced olivine basalts between 2.1 and 0.43 Ma ago, and increasingly differentiated lavas (hawaiite, benmoreite, mugearite and trachyte) until its final activity ca. 27 ka ago (Upton and Wadsworth, 1972; Gillot and Nativel, 1982; Famin et al., 2022). Piton de la Fournaise has been regularly active since at least 400-450 ka (Gillot and Nativel, 1989; Merle et al., 2010) and is still presently in its shield building stage. This volcano, one of the most regularly active of the planet, is well known for producing olivine basalts with little compositional variability (Albarède et al., 1997; Vlastelic et al., 2018).

Mayotte is one of the four islands of the Comoros Archipelago located between Africa and Madagascar (Fig. 1a). The origin of Comoros volcanism is debated and could either be related to a mantle plume or to lihosphere deformation (Hajash and Armstrong, 1972; Emerick and Duncan, 1982; Class et al., 2005; Nougier et al., 1986; Famin et al., 2020; Feuillet et al., 2021; Thinon et al., 2022). The Fani Maoré submarine eruption occurred between 2018 and 2021, 50 km east of Mayotte, along the East-Mayotte submarine Volcanic Chain, on a 3300 m-deep seafloor (Fig. 1c). The eruption produced 6.5 km^3 of homogeneous basanitic magmas during three main eruption phases related to different magma paths (Berthod et al., 2021, 2022; Chauvel et al. 2024).

3. Samples

La Réunion sample set, summarized in Table 1 and displayed in Figure 1b, is composed of: (1) twelve co-genetic samples from the Piton des Neiges differentiation suite, including three olivine-basalts, two hawaiites, two benmoreites and five trachytes. These samples covered all

four magmatic stages of Piton des Neiges (Upton and Wadsworth, 1972; Gillot and Nativel, 1982) and were previously selected and studied by Famin et al. (2016), Nauret et al. (2019), and Berthod et al. (2020) to cover the four magmatic stages of Piton des Neiges volcano. All these samples were collected on land, some emplaced as lava flows and others as sheet intrusions; (2) three plutonic rocks with wehrlitic composition (33 — 41.5 wt% MgO) interpreted as magma chamber cumulates (Barrat and Bachèlery, 2019; Berthod et al., 2020); (3) nine lava samples from the recent (2007-2020) activity of Piton de la Fournaise volcano studied by Vlastelic et al. (2013), including eight basalts with a homogeneous MgO content (6.4 to 8 wt%), and one olivine-rich lava (29.2 wt% MgO). These samples were selected to cover a wide range of textures and cooling rates (crystallized lava, quenched lava, scoria, pumice, Pele's hairs). (4) Ten submarine lavas, including four samples related to the early history of Piton des Neiges, and six lavas related to the submarine volcanism that occurred in the southeast of the island prior to Piton de la Fournaise. These samples have MgO content between 5.1 and 13 wt% (Smietana et al., 2010; Smietana, 2011).

The Fani Maoré samples selected for this study are all fresh submarine lavas studied by Berthod et al. (2021, 2022) and Chauvel et al. (2024). The samples were dredged during MAYOBS (Rinnert et al., 2019) and GEOFLAMME cruises (Rinnert et al., 2021). Dredge locations are reported in Table 1 and displayed in Figure 1c. Samples include: (1) eight evolved basanites covering the three main phases of the 2018-2020 submarine eruption (Table 1). Except for one sample with 9.9 wt% MgO, the eight samples display small compositional variations (3.8 ≤ MgO ≤ 4.8 wt%) ascribed to magma differentiation in a large (≥10 km^3) reservoir located within the lithospheric mantle (Berthod et al., 2021). Bulk porosity decreases from 30 – 45% during phase 1 to 5 – 20% during phase 3 (Verdurme et al., 2024). Sulfides droplets occur in all these samples and are most abundant in the third phase samples (Berthod et al., 2022). (2) Nine samples regularly drilled from the glassy margin to the center of a pillow lava (Fig. 2) erupted during the third phase of the 2018-2021 eruption (sample GFL-DR20-0101 in Berthod et al., 2022, with MgO of 4.45 wt%).

4. Analytical methods

Selenium and tellurium concentrations were analyzed by isotope dilution (ID) hydride generation (HG) quadrupole inductively coupled plasma mass spectrometry (ICP-MS)

following a method modified from Yierpan et al. (2018). We first prepared ^{77}Se enriched (44.773 ppb Se with 94.38% ^{77}Se) and ^{125}Te enriched (5.214 ppb Te with 95.52% ^{125}Te) spike solutions from solid sources obtained from Oak Ridge National Laboratory, USA. The concentrations of the spike solutions were calibrated by isotope dilution against solutions prepared by diluting a 10 μg/g certified standards from Inorganic Venture. The spikes concentrations were obtained by averaging the measurements of three spike-standard mixtures prepared around the spike/standard optimal ratio. For sample analysis, 200 mg of rock powders were weighted in 15 ml Teflon vials. Immediately after, we added between 250 and 500 mg of ^{77}Se enriched spike and between 150 and 300 mg of ^{125}Te enriched spike. The silicates were digested by adding successively 1 ml of 14M HNO_3 and 6 ml of 29M HF and placing the vials on a hotplate at 90°C for 24 hours. The samples were evaporated at 70°C to avoid major Se and Te volatilization (Vlastélic and Piro, 2022). The dry residues were taken in 3 ml of 6M HCl, heated at 90°C for 24H, and evaporated at 70°C. This step of HCl conversion was repeated once. The two-step chemistry from Yierpan et al. (2018) was used to purify Se and Te. The column separation was calibrated by dissolving 320 mg of a La Réunion basalt doped with 500 ng of Se and Te. After HCl conversion, the sample residues were dissolved in 3 ml of 4M HCl, centrifuged for 5 min, before being loaded on anionic columns (polypropylene Biorad filled with 5 ml AG1-X8 100-200 mesh). Most elements and Se were eluted by adding successively 3 x 1 ml and 4 ml of 4M HCl, while Te was retained probably as chloro-complex. Iron was eluted with 2 x 5 ml of 2M HCl – 5M HF and 2 x 3 ml of 0.4M HCl. Tellurium, with minor amount of remaining Pb, was eluted with 6 ml of 0.4M HCl. After evaporation at 65°C, the major element – Se fraction was dissolved in 4 ml of 0.1M HNO_3 and centrifugated before being loaded on cationic columns (polypropylene Biorad filled with 5 ml AG50-X8 200-400 mesh). Selenium was eluted by adding successively 2 x 1 and 3ml of 0.1M HNO_3. The collected Se fraction is not highly pure but is sufficiently depleted in Fe and other transition metals for efficient hydride generation during subsequent ICPMS analysis.

After evaporation at 85°C the fractions of Se (0.14 – 135 ng) and Te (0.04 – 24 ng) recovered from samples were taken in 6 and 3 ml of HNO_3 1M, respectively. The resulting solutions with 0.02- 23 ppb Se and 0.013 – 8 ppb Te were mixed online with 0.3 M $NaBH_4$–0.1 M NaOH in a hydride generation system (HGX-200 from Teledyne Cetac Technologies). The H_2Te and H_2Se vapors were entrained by two Ar flows (carrier flow of 0.42 L/min and make up flow of 0.82 L/min) to an Agilent 7500 ICPMS. To improve ICPMS sensitivity, we used two primary pumps

increasing the vacuum of the interface. $^{78}Se/^{77}Se$ was measured using the reaction cell (He mode) to lower polyatomic interferences from the Ar carrier gas (e.g., $^{40}Ar^{38}Ar^{+}$, $^{36}Ar^{40}Ar^{1}H^{+}$, $^{38}Ar_2{}^{1}H^{+}$), while $^{126}Te/^{125}Te$ was measured in "no-gas" mode. Each measurement included typically 100 scans, with 200 ms acquisition on each mass, and lasted 1 minute. The HNO_3 1M solution used to dissolve samples was repeatedly measured for background correction. Instrumental mass fractionation was corrected by measuring a 5 ppb Se isotopic standard (NIST SRM 3149) and a 1 ppb Te isotopic standard (NIST SRM 3156) at the beginning and/or at the end of each measurement session. Signals of ca. 130 000 CPS/ppb ^{78}Se and 500 000 CPS/ppb ^{126}Te were measured on the NISTs.

Sulfur concentration was measured by isotope dilution using a ^{34}S enriched spike (262 ppm S, with 99.79% ^{34}S). The spike, initially in the form of native sulfur, was dissolved in 14M HNO_3 and calibrated against IAEA-S-1 sulfur isotope reference material. For sample analysis, 50 mg of rock powders were weighted in 15 ml Teflon vials, spiked and digested with 1 ml of 14M HNO_3 and 6 ml of 29M HF at 90°C for 24 hours. After evaporation, the fluoride residue was reduced by addition and evaporation of a few drops of 14M HNO_3. Unlike in the procedure applied by Wang and Becker (2013), sulfur was not separated because of important S release (>1 μg) from the cationic resin. Instead, the residue was taken in 5 ml of H_2O, centrifugated, and $^{32}S/^{34}S$ of the supernatant was directly analyzed on an Element XR ICP-MS in high mass-resolution mode (m/Δm of 10 000). To check the accuracy of S isotope compositions, the $^{32}S/^{34}S$ ratios of a subset of samples from Fani Maoré were also measured as oxides ($^{32}S^{16}O/^{34}S^{16}O$), using the oxygen reactive mode of an Agilent 8900 triple quadrupole ICPMS. Instrumental mass fractionation was corrected by running IAEA-S-1 sulfur isotope reference material. Sample concentration (C_{Sample}) was calculated according to Eq. 1 :

$$C_{Sample} = C_{Spike} \times \frac{m_{Spike}}{m_{Sample}} \times \frac{Ab^{B}_{Spike}}{Ab^{B}_{Sample}} \times \frac{R_{Spike} - R_{mes}}{R_{mes} - R_{Sample}} \qquad (1)$$

Where C_{spike} is the spike concentration, m_{spike} and m_{sample} are the spike and sample masses, R_{spike}, R_{sample} and R_{mes} are the isotopic ratios of the spike, the sample and the measured sample-spike mixture, respectively. R_{sample} being not measured, we use the natural abundances of Se ant Te isotopes of the NIST standards. Ab^{B} is the isotopic abundance of the denominator isotope. The precision of isotopic ratios measured by ICPMS are on the order of

1-3 %. The precision of the concentrations obtained by isotope dilution is inferred from the error magnification (M), defined as (Eq. 2) :

$$M = \frac{\Delta C_{Sample}}{C_{Sample}} / \frac{\Delta R_{mes}}{R_{mes}} = \frac{R_{mes}.(R_{Spike}-R_{Sample})}{(R_{Spike}-R_{mes}).(R_{mes}-R_{Sample})} \quad (2)$$

Error magnification ranges between 1.03 and 1.3 for most samples and reaches 2-3 for the most depleted (olivine-rich basalt) or enriched (Réunion pumice and Pele's hairs) samples. Average procedural blanks are 0.8 ng S, 0.2 ng Se and 0.05 ng Te. The concentrations of the four reference basalts measured during this study (BHVO-2, BCR-2, BEN and BIR-1, Table 2) fall within the range of the recommended values reported in the GeoRem database (Jochum et al. 2005). However, our S value of BIR-1 (4.4 ppm) is much lower than the information value of 70 ppm. Réunion samples that were not previously analyzed for major and trace elements were analyzed conventionally at LMV by ICP-AES (major elements) and ICPMS (trace elements) using the methods described in Gurioli et al. (2018) and Vlastélic et al. (2013), respectively. The only difference is that the plutonic rocks were dissolved using NH_4-HF_2 instead of HF-HNO_3 for ICPMS analysis to ensure complete dissolution.

5. Results

The concentrations of S, Se and Te of La Réunion and Fani Maoré samples are reported in Table 2. Major element and trace element data are reported in supplementary Table S1.

5.1. S – Se – Te budget of La Reunion plutonic rocks

The Piton des Neiges wehrlites (SAL206 and CB150914) have 264-358 ppm S, 19-36 ppb Se and 2.7-3.1 ppb Te. They show S/Se ratios (9985-16966) higher than La Réunion lavas and mantle peridotites (S/Se<8000) but preserve similar Se/Te ratios (6.1 - 13.2) (Fig. 3). The Piton de la Fournaise wehrlite (CHI-7) has 12.7 ppm S, 9.96 ppb Se and 2.56 ppb Te and plot within the compositional field of mantle peridotites (Fig. 3) (Lorand and Alard, 2010; Wang and Becker, 2013). The S/Se (1275) and Se/Te (3.9) ratios of this sample are significantly lower than in carbonaceous chondrites.

250

251 5.2. Differentiation of La Réunion and Mayotte magmas

252

253 Major element and trace element variations during the differentiation of La Réunion and
254 Mayotte magmas are shown in Figure 4. The Réunion samples show four evolution steps,
255 described in Fig. 4 caption, which are consistent with the sequence of low-pressure
256 crystallization of La Réunion magmas (e.g., Villemant et al. 2009; Pichavant et al. 2016).
257 Compared to La Reunion lavas, Fani Maoré lavas are characterized by lower Sc and V, in
258 keeping with high-pressure fractionation of clinopyroxene (Berthod et al., 2021) (Fig. 4e,f).
259 Fani Maoré lavas also have higher Th at given MgO (Fig. 4h).

260

261 5.3. Evolution of S, Se and Te in La Réunion magmas

262

263 La Réunion lavas are extensively depleted in sulfur (5 - 884 ppm S) compared to primitive
264 melts with up to 1800 ppm S (Bureau et al., 1998; Vigouroux et al., 2009; Di Muro et al., 2016)
265 (Fig. 5a). The least degassed submarine lavas from step 1 with 416 – 632 ppm S have already
266 lost between 65 and 77% S, while submarine lava from step 2 (119 – 146 ppm) have lost 92 %
267 of S mostly through degassing because the magmas are not yet sulfide saturated (Fig. 5a). In
268 subaerial conditions, lavas from step 1 (30 – 266 ppm S) have 36 to 95% less S than their
269 submarine counterpart, while lavas from steps 3 and 4 are even more depleted with 5 – 168
270 ppm S. Generally, sulfur concentration shows some scattering in subaerial lavas, and there is
271 only a rough trend of decreasing S with decreasing MgO.

272

273 In submarine environment, selenium displays a similar behavior as sulfur with relatively
274 uniform concentrations (74 – 131 ppb Se) in lavas from step 1 and lower concentrations (34 –
275 51 ppb Se) in lavas from step 2 (Fig. 5b). Unlike sulfur, the selenium contents of subaerial (121
276 ± 21 ppb, n=10) and submarine lavas (104 ± 16 ppb, n=8) from step 1 are similar. The absence
277 of subaerial degassing of Se results in a smooth trend of decreasing Se with decreasing MgO
278 in subaerial samples from Piton des Neiges, with less than 3 ppb Se in the most differentiated
279 samples (Fig. 5b). Most lavas plot within a narrow range of S/Se (2300 — 5000), close to the
280 chondritic value (2750 ± 200), except for subaerial lavas with 4 – 8 wt% MgO where S/Se
281 decreases down to 400 due to degassing loss of S (Fig. 5d). The Cu/Se ratio is relatively uniform

(605 – 1234) in subaerial and submarine lavas from step 1, but markedly increases up to 3010 in the submarine lavas from stage 2 (Fig. 5e). This increase must reflect Se degassing because Cu remains elevated during step 2 (Fig. 4d). The Cu/Se ratio then drops to 89 during step 3 and early step 4 due to sulfide saturation. During late step 4 (<2.5 wt% MgO), Cu/Se increases again up to 9029 due to extensive Se degassing.

Tellurium shows more complex variations (Fig. 5c). The tellurium concentrations of submarine lavas first decrease from 12.4 to 3.7 ppb as MgO decreases from 13 to 7.6 wt%, before increasing abruptly until the end of step 1 (6 wt% MgO) where Te reaches 62 ppb. Then, Te concentrations decrease again during stage 2, while remaining elevated (23 – 33 ppb). Samples collected on land show a very different behavior, with a marked decrease of Te at the end of step 1, from 2.95 to 0.38 ppb. Only sample SAL 51 seems to plot on the submarine trends, possibly because this dyke sample emplaced under elevated pressure. An event of Te increase above 1 ppb occurs during step 3, or early step 4, before the final decrease of Te down to 0.2 ppb. The large variations of Se/Te (1 — 225) between 5 and 8 wt% MgO (Fig. 5f) are mostly due to the large variations of Te between Te-depleted subaerial and Te-enriched submarine lavas (Fig. 5c), while Se remains relatively uniform (Fig. 5b).

Noteworthy, a few samples with biased compositions plot outside the frame of Fig. 5 or are highlighted: (1) The picritic sample (070408-1b) with 29.2% wt% MgO has low S (24 ppm), Se (59 ppb) and Te (0.69 ppb) contents due to the occurrence of olivine crystals highly depleted in S, Se and Te. Yet this sample has Se/Te (86) within the range of subaerial basalts. (2) Compared to other subaerial samples with identical MgO content, the Pele's hairs sample (200409-6) has 80 times more Te (120 ppb) and 5 times more Se (677 ppb), but similar S concentration (196 ppm), yielding very low S/Se (290) and low Se/Te (5.7) ratios (Fig. 5 d, f). (3) Some of the trachytes from Piton des Neiges (SAL 201 and SAL 203) hosting hydrothermal pyrite have anomalously elevated S (730 – 884 ppm), and to a lesser extent Se (76 – 206 ppb) and Te (1.3 – 2.5 ppb) contents. The occurrence of pyrite increases S/Se up to 9600 (Fig. 5d) but does not seem to drastically fractionate the Se/Te ratios of these samples (58 – 83).

5.4. S – Se – Te signature of 2018-2021 Fani Maoré submarine lavas

All Fani Maoré lavas are enriched in sulfur (1342 – 1711 ppm) compared to La Réunion lavas (Fig. 5a), consistently with the occurrence of droplets of iron sulfide (Berthod et al., 2021). Within the narrow S range, we note a trend of increasing S concentration during the 2018-2021 eruption with 1342 – 1413 ppm during phase 1 (July 2018 - May 2019), 1386 – 1509 ppm during phase 2 (May 2019 - August 2019), and 1712 ppm during phase 3b (October 2020 - January 2021). The S content (1430 ppm) of the magnesian sample DR11-0704 is consistent with other samples produced during phase 2.

Unlike sulfur, the selenium concentration of Fani Maoré lavas (66 – 81 ppb) is only slightly higher than La Réunion subaerial and submarine lavas (38 — 51 ppb) with similar MgO content, excluding samples hosting pyrite (Fig. 5 b). Consequently, Fani Maoré lavas display very elevated S/Se ratios (16929 — 22130) (Fig. 5 d), which increase slightly with decreasing MgO. The tellurium concentrations (4.4 – 13.6 ppb) (Fig. 5 c), and Se/Te ratios (5.1 — 15.6) (Fig. 5 f) of Fani Maoré lavas are within the range of La Réunion submarine lavas. The two most evolved Fani Maoré samples (MgO <3.9 wt%) have distinctly higher Te contents (9.5 — 13.6 ppb) and lower Se/Te ratios (5.1 — 7.2).

5.5. S – Se – Te degassing within the Fani Maoré pillow lava

The studied GFL-DR20-0101 pillow lava presents five concentric layers with distinctive textures (Fig. 2): In the core of the pillow (layer 1), only rare small rounded (<1 mm) vesicles occur. The overlying thick layer 2 shows the occurrence of 1-3 cm pipe vesicles with radial distribution. The number of pipes markedly increases in layer 3. However, closer to the surface where the extent of crystallization decreases, neither vesicles nor degassing pipes occur in the layers 4, 5 and 6. Layer 5 stands out from layer 4 due to the occurrence of glass, while the pillow rim (layer 6) is fully glassy. This textural structure is very similar to that described by Berthod et al. (2022) for a pillow lava erupted earlier during the eruption. More generally, this degassing-crystallization structure is typical of pillows lavas (e.g., Philpotts and Lewis, 1987; Merle et al., 2005).

Variations of S, Se and Te concentrations, and S/Se and Se/Te ratios from pillow rim to pillow core are reported in Figure 6. Sulfur and Se display similar variations, with the base of layer 2 being depleted in S (1518 – 1593 ppm) and Se (76.8 – 77.0 ppb) compared to pillow core (1671 – 1794 ppm S and 82.6-83.5 ppb Se) and external layers (1751– 1881 ppm S and 82.1-83.6 ppb

Se). Sulfur loss (13%) being more important than Se loss (7%), S/Se is lower in layer 2 (19706 – 20738) compared to pillow core (20235 – 21496) and external layers (21243 – 22641). Tellurium displays a different zonation pattern, with low and homogeneous concentrations (4.5 – 4.9 ppb) in the internal layers 1 and 2, and markedly higher concentrations (5.7 – 6.0 ppb) in the external layers 3-6. Consequently, the Se/Te ratio is lower in the external layers (13.8 – 14.7) compared to the internal layers (16.3 – 17.2).

Concentration profiles are also reported for elements showing remarkable variations across the pillow. Like S and Se, Mo and W are markedly depleted (20 – 30%) in the intermediate layer 2 compared to pillow core and rim. Unlike lighter alkali, Cs is also depleted (12%) in the outer part of layer 2. Antinomy is enriched in the outermost layer of the pillow.

6. Discussion

6.1. Processes controlling selenium retention in and degassing from magmas

The drop of sulfur solubility in oxidized melts below 100 MPa (Lesne et al., 2011; Di Muro et al., 2016) explains why sulfur outgassing from submarine lavas increases with decreasing water depth and is extensive in shallow or subaerial lavas. No experimental work has characterized selenium degassing during magma decompression, but several studies of oceanic basalts noted that, unlike sulfur, selenium is retained in seafloor lavas emplaced over a wide depth range (Jenner et al., 2010; Lissner et al., 2014; Yierpan et al. 2019, 2021; Kurzawa et al., 2019). This work shows that moderately differentiated (MgO> 6%) subaerial lavas from La Réunion Island also preserve the same Se content as their submarine counterpart (Fig. 5b), while S is extensively lost (Fig. 5a). Jenner et al. (2010) suggested that selenium must be stabilized in silicate melts as Se^{2-}, in the same manner as sulfur is stabilized as S^{2-}. The stabilization mechanism involves substitution of S^{2-} and Se^{2-} for O^{2-} in the silicate liquid (Wykes et al., 2015). The low volatility of Se during final magma ascent and decompression may be related to the selenide-selenate transition occurring at an oxygen activity > 10^3 higher than the sulfide-sulfate transition. In the relatively oxidized redox conditions of undegassed basaltic magmas (near the nickel nickel-oxide buffer, Moussallam et al. 2016; Pichavant et al., 2016) a large fraction of sulfur occurs as sulfate not stabilized in the silicate melt and thus available for degassing, while selenium still occurs as selenides retained in the silicate melt structure.

During magma differentiation, Se loss starts during step 2, where clinopyroxene and plagioclase join olivine as major fractionating phases, and is extensive during step 4 where sulfide is stable (Fig. 5). This can be explained either by (1) Se degassing and/or (2) the fractionation of a sulfide phase in which Se partition. Note that selenide saturation has hardly any chance to form because Selenium Content at Selenide Saturation (SeCSeS >1000 ppm) is much higher than the total Se budget of magmas (Se < 0.5 ppm) (Wykes et al., 2015). The drop of Se concentration in the most differentiated subaerial lavas from La Réunion Island (Se < 5 ppb for MgO < 2 wt%) contrasts with the subtle Se decrease reported for evolved submarine lavas from convergent margins (Jenner et al., 2015; Kurzawa et al. 2019), where Se remains above 70 ppb even in the most evolved samples. For La Réunion samples, the drop of Se below 4 wt% MgO correlates with a factor of 100 increase of Cu/Se (Fig. 5), from 89 to 9020. Selenium being more volatile than Cu, but less compatible in sulfide, the Cu/Se ratio reflects the contribution of Se degassing (high Cu/Se) relative to sulfide saturation (low Cu/Se). This observation indicates that Se exhaustion in the most evolved Réunion lavas results from extensive degassing, either during shallow magma storage or during eruption.

The question then arises as to how and why Se volatilizes during magma differentiation, while it does not during magma decompression. The critical decrease of Se between 6.0 and 0.5%wt MgO (Fig. 5b) despite the important decrease of the melt fraction (a factor of 6 based on Th increase, Fig. 4h) requires a major drop of Se solubility. Selenium must remain in the form of Se^{2-} in a differentiating melt that becomes increasingly reduced due to SO_2 degassing (Moussallam et al. 2016). If Se^{2-} substitutes for O^{2-} in the melt, it is hypothesized that the Se—(Si, Al) bonds are weaker than the original O—(Si, Al) bonds and are preferentially broken during crystal nucleation and growth, releasing Se. Kinetic might also play a major role because magma storage and differentiation occur over long timescales compared to magma ascent, which inevitably facilitates the diffusion and loss of volatile elements. For instance, it took about 300 ka for Piton des Neiges olivine basalts to evolve into trachyte (Upton and Wadsworth, 1972; Gillot and Nativel, 1982), whereas Piton de la Fournaise magmas can ascend from crustal reservoirs to the surface in a matter of days (Battaglia et al., 2005). Between these two end-member cases, variable Se loss is expected in the current steady-state regime of Piton de la Fournaise, where magma undergo static degassing during its storage at different depths before being by rapidly extruded. Interestingly, S/Se is little fractionated in

410 the most differentiated subaerial lavas (MgO< 4 wt%). This suggests that in the reducing
411 conditions of differentiated magmas, sulfur dominantly occurs as S^{2-} and follows the same
412 degassing processes as Se. However, detailed inspection of the data (Fig. 5) reveals a slight
413 decrease of S/Se in the most differentiated samples (step 4), in keeping with the high S/Se of
414 cumulative rocks (Fig. 3) where sulfides accumulate (Upton et al., 2000).
415
416 6.2. Tellurium specific behavior
417
418 As for sulfur, tellurium is extensively lost from subaerial lava, with nearly no overlap between
419 Te-depleted subaerial lavas and Te-enriched submarine enriched lavas: in the Réunion-
420 Mayotte data set, 18 out of the 20 subaerial samples have less than 3.5 ppb Te, whereas all
421 the submarine lavas (20) have more than 3.5 ppb Te. This feature is also generally seen in the
422 global OIB data set (Yi, 2000; Forrest et al., 2017, Yierpan et al., 2021), although some well-
423 documented subaerial basalts from Hawaii (BHVO2 from Kilauea with 14.2 ppb Te) or Iceland
424 (BIR-1 from Iceland with 5.8 ppb Te) have similar Te content as their submarine counterparts
425 (Yierpan et al., 2018). Like S and Se, Te^{2-} solubilizes in silicate melt by replacing O^{2-} (Renggli et
426 al, 2022). The telluride – tellurate transition being close to the sulfide – sulfate transition along
427 the oxygen fugacity scale (McPhail et al., 1995), only a fraction of Te occurs as soluble Te^{2-} in
428 the redox conditions of basaltic magmas. Thus, Te exsolution and volatilization at atmospheric
429 pressure might thus result from partial oxidation, as for sulfur.
430 During the crystallization sequence of La Réunion magmas, major degassing-induced loss of
431 Te (from 2.9 to 0.38 ppb) occurs in subaerial lavas between MgO of 8.2 and 5 wt%.
432 Remarkably, over the same MgO range where Te is extensively lost from subaerial lavas, the
433 Te content of submarine lavas rises from 3.7 to 62 ppb Te, exceeding the highest
434 concentrations reported so far in submarine basalts (29.2 ppb Te in one sample from Loihi
435 seamount, Hawaii, Yi et al., 2000)). Such enrichment cannot be explained by crystallization
436 alone because the concentration of highly incompatible elements, like Th, increases by no
437 more than 50%. Another possibility is that the most elevated Te concentrations of submarine
438 basalts result from sample contamination with seawater derived Fe-Mn oxides, in which Te is
439 enriched more than any other elements relative to Earth crust (Hein et al., 2003). However,
440 we consider this possibility as unlikely because (i) the whole rock powders analyzed were
441 made from the interior of the pillow lavas (Smietana, 2011), and (ii) elements highly enriched

in Fe-Mn crusts, such as Mn and Co, do not show anomalous concentrations in the Te-enriched sampled. Instead, the anomalous Te increase correlates with a marked increases of the metalloids As (from 1 to 13.8 ppm) and Sb (from 0.1 to 1 ppm), suggesting that Te is mobilized and enriched by degassing processes. We also note that, despite very different volcanic and petrologic contexts, Te concentration also anomalously increase in the most differentiated lavas from the Fani Maoré eruption (Fig. 5c), hence pointing to a general process. We hypothesize that Te enrichment at some steps of magma evolution could result from Te exsolution from deep melts, transfer and accumulation in magmas stored at shallower depth, in a similar manner as CO_2 fluxing (Blundy et al., 2010). Such process is supported by the lower solubility of Te in silicate melts compared to S and Se (Helmy et al., 2020). Alternatively, Te accumulation could occur after eruption at the surface of thick lavas flows that undergo internal differentiation and degassing. Such process has been shown to occur for Li, B and Cs (Kuritani and Nakamura, 2006), and is not inconsistent with the fact that the surface of submarine lavas flow is preferentially sampled during dredging. In both cases, extensive degassing of Te in subaerial setting is expected to prevent Te accumulation in the lavas.

6.3. Assessment of S – Se – Te degassing during the emplacement of Fani Maoré submarine lavas

Pillow lava degassing is a complex process due to the opposite effects of rim quenching and progressive crystallization of is interior. Previous studies reported differences in S, Se and Te concentrations between pillow interiors and glassy rims (Lissner 2014; Forrest et al. 2017). They noted that sulfur concentration is generally lower in pillow interiors, and that the difference between rim and interior is less systematic for Se, and especially for Te. The compositional profile reported here for a sample from the Fani Maoré eruption provides a more detailed view on pillow degassing, revealing that only the intermediate layer of the pillow hosting pipes vesicles is extensively outgassed in S and Se. Pipes vesicles are the textural remnants of the internal degassing of pillow lavas. They are though to form by exsolution of gas from crystallizing magma onto bubbles attached to the advancing solidification front (Philpotts and Lewis, 1987). Merle et al. (2005) estimated that at least 25 vol% crystallization is necessary to produce a crystal framework required for generating the segregation structures in pillows. In the studied differentiated Fani Maoré sample (MgO of 4.45 wt%), pipe

vesicles are not rooted deep in the pillow, which explains the degassing of the intermediate layer mainly. Unlike S and Se, Te is depleted in both layers 1 and 2, showing a zonation (Fig. 6) unrelated to the pipe vesicles. This suggests that Te does not behaves as major volatile species. To explain Te degassing of layer 1 in the absence of degassing pipes, it is hypothesized that Te is less soluble than major volatile species in silicate melts and is lost earlier by diffusion. In support of this possibility, Te is less soluble than S and Se in silicate melts saturated in sulfide, selenide and telluride (Helmy et al., 2020).

The compositional profile reported on Fig. 6 allows an assessment of pillow degassing during emplacement and cooling. The sample was divided into nine shells (s) corresponding to the nine analyzes. The boundary between each shell was set at equal distance between neighboring drill holes (Fig. 2). The volume of each shell (V_s) was calculated assuming a spherical geometry. The density (ρ) of the pillow was assumed to be uniform (ρ_s=ρ_{tot}). At the scale of the pillow, the mass fraction of element lost by degassing (ε) is calculated according to (Eq. 3):

$$\varepsilon_x = 1 - \frac{\sum_{s=1}^{s=9}[X]_s \times V_s \times \rho_s}{[X]_{max} \times V_{tot} \times \rho_{tot}}$$

Where $[X]_s$ is the element concentration in shell s, and $[X]_{max}$ is the highest concentration measured in the pillow thought to be close to the pre-eruptive value. Values of ε are 6.5% for S, 7.2% for Te, but only 1.6% for Se confirming the lower volatility of Se during lava emplacement. Chalcogens degassing is accompanied with significant loss of W (ε = 8.9%), Mo (ε =5.1%) and Cs (ε = 5.1%), which appear to be much more volatile than during subaerial eruptions where ε is lower than 0.15% for those elements (Rubin et al., 1997). W and Mo are highly refractory elements, but their oxides are known to volatilize readily at 1000°C and 1 atmosphere pressure in the presence of water vapor (Millner and Neugebauer, 1949), and this effect is expected to increase with pressure. Thus, water exsolution from the pillow seems to have played a role in mobilizing refractory elements. Between 2018 and 2020, the Fani Maoré submarine eruption produced 6.5 km^3 of lava with an average vesicularity of 27% (i.e., 4.8 km^3 of dense rock) (Berthod et al., 2021). Using a dense rock density of 2500 kg/m3 (Verdurme et al., 2024) and the highest element concentrations of the three eruptive phases as reference, it is estimated from the ε values that the Fani Maoré eruption released 1.1 – 1.5 x 10^6 tons of

505 S, 2300 – 2700 tons of Mo, 970 – 1130 tons of W, 194 – 339 tons of Cs, 13.3 – 16 tons of Se
506 and 4.5 – 11.8 tons of Te. By comparison the Se amount released in the ocean by the Fani
507 Maoré eruption between 2018 and 2021 corresponds to 1% of the degassing fluxes of mid-
508 ocean ridges (Rubin et al., 1997).
509
510 6.4. Brief constraints on magma sources
511
512 The elevated S/Se ratios of the two Piton des Neiges wehrlites confirm previous field and
513 petrological evidences (Berthod et al., 2020) that the samples formed at the bottom of a
514 magma chamber where they accumulated dense sulfides (Fig. 3). Conversely, the S – Se – Te
515 signature of Piton de la Fournaise wehrlite (CHI-7) is consistent with a mantle origin. Its low
516 S/Se and Se/Te ratios relative to the Bulk Silicate Earth (BSE) (Fig. 3), together with its
517 depletion in incompatible elements (Table S1), indicate that this sample is a mantle residue
518 after melt extraction. To reconstruct the possible composition of the parental fertile
519 peridotite, the CHI-7 melting residue is mixed with the extracted melts, best represented by
520 the erupted lavas. The resulting mixing curve intercept the BSE composition (Fig. 3), raising
521 the possibility that the La Réunion plume source preserved the same S/Se and Se/Te ratios as
522 the BSE and CI chondrites. This agrees with previous inferences from Highly Siderophile
523 Elements (Peters et al., 2016) and U-Th-Pb isotope systematics (Vlastélic et al., 2006) that the
524 Réunion plume samples a less differentiated mantle domain.
525 All Fani Maoré lavas including the magnesian sample (MAY04-DR11-0704) display S/Se ratios
526 (16929 — 22130) that are much higher than in worldwide MORB and OIB (S/Se < 10000). The
527 S/Se ratios of Fani Maoré lavas are also higher than the most fertile mantle peridotites
528 (S/Se~8000) (Wang and Becker, 2013) and the two cumulative rocks from La Réunion (S/Se
529 10000<S/Se<14000), which are known to be enriched in sinking sulfur liquids (Upton et al.,
530 2000). Fani Maoré's S – Se signature is hardly explained by magma generation processes and
531 must reflect a source property. The most likely explanation is that the Fani Maoré lavas derive
532 from the melting of a lithospheric mantle extensively refertilized by sulfide melts. This is not
533 inconsistent with previous inferences that the Fani Maoré volcano, like the island of Mayotte,
534 formed by melting of a carbonated mantle source enriched in Ba and volatiles (Chauvel et al.
535 2024; Pelleter et al. 2014). Lithosphere refertilization is a common process driven by repeated

536 melt intrusions, but in the case of the Fani Maoré volcano, it might have reached an unusual
537 extent and caused this exceptionally large-volume eruption.
538
539 7. Conclusions
540
541 This work obtained the following results:
542 (1) Unlike sulfur, selenium degassing is not significant during the final (30 – 0.1 MPa),
543 presumably rapid ascent of moderately differentiated (MgO > 6wt%) magmas from La
544 Réunion. Conversely, selenium degassing occurs during magma differentiation below 6 wt%
545 MgO, at a similar rate as sulfur, yielding small S/Se fractionation in the residual magma. The
546 long timescales require to markedly differentiate La Réunion magmas certainly facilitates the
547 diffusion and loss of less volatile selenium. Variable Se loss is expected in the intermediate
548 situations involving both static degassing during more or less prolonged magma storage
549 followed by rapid extrusion of magma.
550 (2) During the evolution of La Réunion magma reservoir, the onset of sulfide saturation occurs
551 between ~5 and ~4 wt% MgO, while olivine just left the liquidus, and Ti-magnetite has not yet
552 appeared. Sulfide fractionation controls Cu/Se variations over this narrow MgO range, while
553 degassing dominates outside.
554 (3) As sulfur, tellurium is extensively lost from La Réunion subaerial lavas, whereas submarine
555 lavas tend to retain Te and possibility accumulate Te near 6% MgO. The contrasted behavior
556 of Se and Te yields extremely large Se/Te variations between subaerial (up to 225) and
557 submarine (down to 1.0) lavas.
558 (4) A pillow lava emplaced during the Fani Maoré eruption offshore Mayotte shows degassing-
559 driven radial compositional zonation. Degassing of S, Se and other moderately volatile
560 elements (Mo, W, Cs) is the most important at intermediate depth within the pillow where
561 pipe vesicle occur, suggesting they escape with major volatiles. Conversely, Te is depleted in
562 the whole interior of the pillow, suggesting Te degassing through other means.
563 (5) Assessment of pillow degassing during emplacement yields losses of 6.5% for S, 7.2% for
564 Te, but only 1.6% for Se confirming the lower volatility of Se during lava emplacement.
565 Chalcogens degassing is accompanied with significant loss of W (8.9%), Mo (5.1%) and Cs
566 (5.1%). Based on these values, the 6.5 km^3 Fani Maoré eruption released 1.1 – 1.5 x 10^6 tons

of S, 2300 – 2700 tons of Mo, 970 – 1130 tons of W, 194 – 339 tons of Cs, 13.3 – 16 tons of Se and 4.5 – 11.8 tons of Te during emplacement.

(6) The reconstructed S – Se – Te composition of La Réunion plume source is consistent with the preservation of chondritic S/Se and Se/Te ratios, in agreement with previous suggestions that the Réunion plume samples a less differentiated mantle domain.

(7) The unusually elevated S/Se ratios (16929 — 22130) of Fani Maoré lavas suggests that the mantle source of this exceptional eruption has been extensively fertilized by sulfide melts.

Figure captions

Figure 1. Location maps. (a) Relief map of the southwest Indian Ocean showing the locations of La Réunion and Mayotte islands. (b) Relief map of La Réunion Island showing the location of the Piton des Neiges and Piton de la Fournaise volcanoes, and the location of subaerial and submarine samples analyzed in this study. Closed triangles: Piton des Neiges lavas; closed circles: Piton de la Fournaise lavas; closed hexagons: cumulates ; closed diamond: peridotite, open circles: submarine lavas. (c) Relief map of Mayotte Island, showing the locations of the samples from the Fani Maoré submarine eruption (open diamonds) that occurred between 2018 and 2021 50 km east of Mayotte island, along the East-Mayotte submarine Volcanic Chain. All maps done with GeoMapApp (https://www.geomapapp.org/).

Figure 2. Cross section of GFL-DR20-0101 pillow lava emplaced during phase 3 of the Fani Maoré eruption. Drill holes are shown and numbered from pillow interior (DR20-1) to pillow rim (DR20-12). Pillow surface (DR20-Sp) is the thin external glassy layer not shown here (layer 6). The five main textural unit (1-5) described in text are shown. Because the external layers 4 and 5 are thinner than other layers, between 3 and 4 smaller drill holes were made and mixed within each layer.

Figure 3. Composition of La Réunion plutonic rocks reported in (a) S/Se and (b) Se/Te versus Al_2O_3 plots. The compositional field of mantle peridotites, and the composition of carbonaceous chondrites (CI) and Bulk Silicate Earth (BSE) are shown (Lorand and Alard, 2010; König et al., 2012; Wang and Becker, 2013). Closed hexagons: cumulates; closed diamond: peridotite. Analytical error is smaller than symbols size. Data are from Table 2 (S, Se and Te concentrations) and supplementary Table S1 (Al_2O_3 concentrations). The dashed line is a mixing curve calculated by mixing CHI-7 peridotite with the less degassed submarine DR6-2 lava sample, which is representative of the most common composition of La Réunion volcanism.

Figure 4. Major-trace elements versus MgO plot showing the composition of La Réunion and Fani Maoré lavas. Vertical thin lines indicate major changes in the crystallization assemblage. The crystallization sequences of La Réunion magma involves four steps (Villemant et al. 2009;

607 Pichavant et al. 2016) : (1) primary melts (MgO≥9%) first crystallize olivine and spinel causing
608 an important decrease of Ni and Cr; (2) Clinopyroxene and plagioclase appear at the liquidus
609 at MgO~6 wt% as recorded by the onset of Sc, V and Ca/Al decrease. (3) Between ~5 and ~4
610 wt% MgO, the increase of Fe and Ti indicate that olivine is no longer a liquidus phase, while
611 Ti-magnetite has not yet appeared. The abrupt drop of Cu (from 97 to 18 ppm) indicates that
612 the onset of sulfide saturation occurs at this step. This corresponds to the first phase of sulfide
613 formation which is triggered by S becoming saturated in magmas (Collins et al. 2012). (4)
614 Below ~4 wt% MgO, the decrease of Fe, Ti, Ca/Al, Sc and Cu, and the increase of Th are
615 consistent with precipitation of clinopyroxene, plagioclase, magnetite and sulfides. This
616 second phase of sulfide saturation is related to the crystallization of titanomagnetite which
617 reduces the sulfur content at sulfide melt saturation (Jenner et al., 2010; Collins et al. 2012).
618 The crystallization assemblage of Fani Maoré samples (80% Cpx – 20 % Ol) is from Berthod et
619 al. (2021). Symbols are as in previous figures. Data are from Table 2 (S, Se and Te
620 concentrations) and supplementary Table S1 (major and trace element concentrations from
621 La Réunion samples). Fani Maoré data are from Berthod et al. (2022) (major elements) and
622 Chauvel et al. (2024) (trace elements). Fani Maoré trace element data not given in Chauvel et
623 al. (2024) were taken from Berthod et al. (2022).
624
625 Figure 5. Chalcogen contents (S, Se, Te) and ratios (S/Se, Cu/Se, Se/Te) plotted against MgO
626 content of lavas. Vertical thin lines indicate major changes in the mineral assemblage
627 crystallizing (see figure 4). The composition of La Réunion and Fani Maoré lavas are reported
628 using the same symbols as in previous figures. Analytical error is smaller than symbols size.
629 Data are from Table 2 (S, Se and Te concentrations) and supplementary Table S1 (MgO and Cu
630 concentrations from La Réunion samples). Fani Maoré data are from Chauvel et al. (2024) (Cu)
631 and Berthod et al. (2022) (MgO and Cu).
632
633 Figure 6.
634 Radial compositional zonation of GFL-DR20-0101 pillow lava emplaced during the third and
635 last phase (October 2020 - January 2021) of the Fani Maoré eruption (Berthod et al., 2020).
636 Vertical dashed lines separate the major textural units shown in figure 2 and described in text.
637 Error bars are indicated or smaller than symbols size. Data are from Table 2 and
638 supplementary Table S1.

639 **References**

640

641 Albarède, F., Luais, B., Fitton, G., Semet, M., Kaminski, E., Upton, B. G. J., Bachèlery, P.,
642 Cheminée, J. L., 1997. The geochemical regimes of Piton de la Fournaise volcano
643 (Réunion) during the last 530 000 years. J. Petrol. 38, 171–201.

644 Battaglia, J., Ferrazzini, V., Staudacher, T., Aki, K., Cheminée, J.-L., 2005. Pre-eruptive migration
645 of earthquakes at the Piton de la Fournaise volcano (Réunion Island). Geophys. J. Int.
646 161, 549–558.

647 Barrat J.-A., Bachèlery Patrick, 2019. La Réunion Island dunites as analogs of the Martian
648 chassignites: Tracking trapped melts with incompatible trace elements, Lithos 344–
649 345, 452-463.

650 Berthod, C., Michon, L., Famin, V., Welsch, B., Bachèlery, P., Bascou, J., 2020. Layered gabbros
651 and peridotites from Piton des Neiges volcano, La Réunion Island. J. Volcanol.
652 Geotherm. Res. 405, 107039.

653 Berthod, C., et al., 2021. The 2018-ongoing Mayotte submarine eruption: Magma migration
654 imaged by petrological monitoring. Earth Planet. Sci. Lett. 571, 117085.

655 Berthod, C., et al., 2022. Temporal magmatic evolution of the Fani Maoré submarine eruption
656 50 km east of Mayotte revealed by in situ sampling and petrological monitoring.
657 Collect. C R Geosci. 354 (S2), 195–223.

658 Blundy, J., Cashman, K.V., Rust, A., Witham, F., 2010. A case for CO2-rich arc magmas. Earth
659 Planet. Sci. Lett. 290, 289-301.

660 Bonneville, A., Barriot, J.P., Bayer, R. (1988) Evidence from geoid data of a hotspot origin for
661 the southern Mascarene Plateau and Mascarene Islands, (Indian Ocean). J Geophys
662 Res 93, 4199–4212.

663 Bureau, H., Pineau, F., Métrich, N., Semet, M.P., Javoy, M. (1998). A melt and fluid inclusion
664 study of the gas phase at Piton de la Fournaise volcano (Reunion Island). Chem. Geol.
665 147, 115-130.

666 Chauvel, C., Inglis, E. C., Gutierrez, P., Luu T.-H., Burckel P., Besson P., 2024. Fani Maoré, a new
667 “young HIMU” volcano with extreme geochemistry, Earth Planet. Sci. Lett. 626,
668 118529.

669 Class, C., Goldstein, S., Stute, M., Kurz, M., Schlosser, P., 2005. Grand Comore Island: A well-
670 constrained “low 3He/4He” mantle plume. Earth Planet. Sci. Lett. 233, 391–409.

671 Collins, S.J., Maclennan, J., Pyle, D.M., Barnes, S.J., Upton, B.G.J., 2012. Two phases of sulphide
672 saturation in Reunion magma: evidence from cumulates. Earth Planet. Sci. Lett. 337–
673 338, 104–113.
674 Deniel, C., Kieffer, G., Lecointre, J., 1992. New 230Th–238U and 14C age determinations from
675 Piton des Neiges volcano, Reunion—A revised chronology for the Differentiated Series.
676 J. Volcanol. Geotherm. Res. 51, 253–267.
677 Di Muro, A., Métrich, N., Allard, P., Aiuppa, A., Burton, M., Galle, B. (2016). Magma degassing
678 at Piton de la Fournaise Volcano. In: Active Volcanoes of the Southwest Indian Ocean.
679 Springer, Berlin, Heidelberg, pp.203–222.
680 Edmonds M., Mather T.A., Liu E.J., 2018. A distinct metal fingerprint in arc volcanic emissions.
681 Nat. Geosci. 11, 790–794.
682 Emerick, C.M., Duncan, R.A., 1982. Age progressive volcanism in the Comores Archipelago,
683 western Indian Ocean and implications for Somali plate tectonics. Earth Planet. Sci.
684 Lett. 60, 415–428.
685 Famin, V., C. Berthod, L. Michon, J. Eychenne, E. Brothelande, M.-M. Mahabot, M. Chaput,
686 2016. Localization of magma injections, hydrothermal alteration, and deformation in a
687 volcanic detachment (Piton des Neiges, La Réunion). J. Geodynamics 101, 155-169.
688 Famin, V., Michon, L., Bourhane, A., 2020. The Comoros archipelago: a right-lateral transform
689 boundary between the Somalia and Lwandle plates. Tectonophysics 789, 228539.
690 Famin, V., C. Paquez, M. Danišík, N. J. Gardiner, L. Michon, C. K. Kirkland, C. Berthod, B.
691 Friedrichs, A. K. Schmitt, P. Monié, 2022. Multi-technique Geochronology of Intrusive
692 and Explosive Activity on Piton des Neiges Volcano, Réunion Island. Geochem.
693 Geophys. Geosyst. 23, e2021GC010214.
694 Feuillet, N., Jorry, S., Crawford, W.C., Deplus, C., Thinon, I., Jacques, E., Saurel, J.M., Lemoine,
695 A., Paquet, F., Satriano, C., Aiken, C., Foix, O., Kowalski, P., Laurent, A., Rinnert, E.,
696 Cathalot, C., Donval, J.-P., Guyader, V., Gaillot, A., Scalabrin, C., Moreira, M., Peltier, A.,
697 Beauducel, F., Grandin, R., Ballu, V., Daniel, R., Pelleau, P., Gomez, J., Besançon, S., Geli,
698 L., Bernard, P., Bachelery, P., Fouquet, Y., Bertil, D., Lemarchand, A., Van der Woerd,
699 J., 2021. Birth of a large volcanic edifice offshore Mayotte via lithosphere-scale dyke
700 intrusion. Nat. Geosci. 14, 787–795.

Forrest, A., Kelley K.A., Schilling J.G., 2017. Selenium, tellurium and sulfur variations in basalts along the Reykjanes Ridge and extension over Iceland, from 50°N to 65°N. Interdisciplinary Earth Data Alliance (IEDA). doi: 10.1594/IEDA/100700.

Gillot, P.-Y., Nativel, P., 1982. K-Ar chronology of the ultimate activity of Piton des Neiges volcano, Reunion Island, Indian Ocean. J. Volcanol. Geotherm. Res. 13, 131–146.

Gillot, P.-Y., Nativel, P.-E., 1989. Eruptive history of the Piton de la Fournaise volcano, Réunion Island, Indian Ocean. J. Volcanol. Geotherm. Res. 36, 53–65.

Gurioli, L., Di Muro, A., Vlastélic, I., Moune, S., Villeneuve, N., Bachèlery, P., Valer, M., Thivet, S., Boudoire, G., Peltier, A., Ferrazzini, V., Métrich, N., Benbakkar, M., Cluzel, N., Constantin, C., Devidal, J.-L., Fonquernie, C., Hénot, J.-M., 2018. Integrating field, textural and geochemical monitoring to track eruption triggers and dynamics: a case-study from Piton de la Fournaise, Solid Earth, 9, 431–455.

Greenland, L.P., Aruscavage, P., 1986. Volcanic emission of Se, Te, and As from Kilauea volcano, Hawaii. J. Volcanol. Geotherm. Res. 27, 195-201.

Hajash, A., Armstrong, R.L., 1972. Paleomagnetic and radiometric evidence for the age of the Comores Islands, west central Indian Ocean. Earth Planet. Sci. Lett. 16, 231–236.

Hein, J.R., Koschinsky A., Halliday A.N., 2003. Global occurrence of tellurium-rich ferromanganese crusts and a model for the enrichment of tellurium. Geochim. Cosmochim. Acta 67, 1117–1127.

Helmy, H.M., Ballhaus, C., Fonseca, R.O.C., Leitzke, F.P. (2020). Concentrations of Pt, Pd, S, As, Se and Te in silicate melts at sulfide, arsenide, selenide and telluride saturation: evidence of PGE complexing in silicate melts? Contrib. Mineral. Petrol. 175, 65.

Hertogen, J., Janssens, M.-J., Palme, H. (1980) Trace elements in ocean ridge basalt glasses: implications for fractionations during mantle evolution and petrogenesis. Geochim. Cosmochim. Acta 44, 2125-2143.

Jenner, F.E., Hauri, E.H., Bullock, E.S., König, S., Arculus, R. J., Mavrogenes, J. A., Mikkelson, N., Goddard, C., 2015. The competing effects of sulfide saturation versus degassing on the behavior of the chalcophile elements during the differentiation of hydrous melts, Geochem. Geophys. Geosyst., 16, 1490–1507, doi:10.1002/2014GC005670.

Jochum, K.P., Nohl, U., Herwig, K., Lammel, E., Stoll, B., Hofmann A.W., 2005. GeoReM: A New Geochemical Database for Reference Materials and Isotopic Standards. Geostand. Geoanal. Res. 29, 333-338.

König, S., Luguet, A., Lorand, J.-P., Wombacher, F., Lissner, M., 2012. Selenium and tellurium systematics of the Earth's mantle from high precision analyses of ultradepleted orogenic peridotites. Geochim. Cosmochim. Acta 86, 354–366.

Kuritani, T., Nakamura, E., 2006. Elemental fractionation in lavas during post-eruptive degassing: Evidence from trachytic lavas, Rishiri Volcano, Japan. J. Volcanol. Geotherm. Res. 149, 124– 138.

Kurzawa, T., König, S., Alt, J.C., Yierpan, A., Schoenberg, R., 2019. The role of subduction recycling on the selenium isotope signature of the mantle: Constraints from Mariana arc lavas. Chem. Geol. 513, 239–249.

Jenner, F.E., O'Neill, H.S.C., Arculus, R.J. and Mavrogenes, J.A., 2010. The magnetite crisis in the evolution of Arc-related magmas and the initial concentration of Au, Ag and Cu. J. Petrol. 51, 2445–2464.

Lesne, P., Kohn, S. C., Blundy, J., Witham, F., Botcharnikov, R. E., Behrens, H., 2011. Experimental simulation of closed-system degassing in the system basalt-H2O–CO2–S–Cl. J. Petrol. 52, 1737–1762.

Lissner, M., König, S., Luguet, A., le Roux, P.-J., Schuth, S., Heuser, A., le Roex, A.-P., 2014. Selenium and tellurium systematics in MORBs from the southern Mid-Atlantic Ridge (47–50°S). Geochim. Cosmochim. Acta 144, 379–402.

Lorand J.-P., Alard O., 2010. Determination of selenium and tellurium concentrations in Pyrenean peridotites (Ariege, France): new insight into S/Se/Te systematics of the upper in mantle samples. Chem. Geol. 278, 120–130.

McPhail, D.C., 1995. Thermodynamic properties of aqueous tellurium species between 25 and 350 C. Geochim. Cosmochim. Acta 59, 851–866.

Merle, R., Caroff, M., Girardeau, J., Cotton, J., Guivel, C., 2005. Segregation vesicles, cylinders, and sheets in vapor-differentiated pillow lavas: examples from Tore-Madeira Rise and Chile Triple Junction, J. Volcanol. Geotherm. Res. 141, 109-122.

Merle, O., Mairine, P., Michon, L, Bachèlery, P., Smietana, M. (2010) Calderas, landslides and paleo-canyons on Piton de la Fournaise volcano (La Réunion Island, Indian Ocean). J Volcanol. Geotherm. Res. 189, 131–142.

Millner, T., Neugebauer, J., 1949. Volatility of the Oxides of Tungsten and Molybdenum in the Presence of Water Vapour. Nature, 163, 601-602.

764 Moussallam, Y., Edmonds, M., Scaillet, B., Peters, N., Gennaro, E., Sides, I., Oppenheimer, C.,
765 2016. The impact of degassing on the oxidation state of basaltic magmas: A case study
766 of Kīlauea volcano. Earth Planet. Sci. Lett. 450, 317-325.
767 Nauret, F., Famin, V., Vlastelic, I., Gannoun, A., 2019. A trace of recycled continental crust in
768 the Réunion hotspot. Chem. Geol. 524, 67–76.
769 Nougier, J., Cantagrel, J.M., Karche, J.P., 1986. The Comores archipelago in the western Indian
770 Ocean: volcanology, geochronology and geodynamic setting. J. Afr. Earth Sci. 1983,
771 135–145.
772 Pelleter, A.-A., Caroff, M., Cordier, C., Bachelery, P., Nehlig, P., Debeuf, D., Arnaud, N., 2014.
773 Melilite-bearing lavas in Mayotte (France): An insight into the mantle source below the
774 Comores. Lithos 208–209, 281–297.
775 Peters, B.J., Day, J.M.D., Taylor, L.A., 2016. Early mantle heterogeneities in the Réunion
776 hotspot source inferred from highly siderophile elements in cumulate xenoliths. Earth
777 Planet. Sci. Lett., 448, 150-160.
778 Pichavant, M., Brugier, Y., Di Muro, A., 2016. Petrological and Experimental Constraints on the
779 Evolution of Piton de la Fournaise Magmas. In: Bachelery, P., Lenat, JF., Di Muro, A.,
780 Michon, L. (eds) Active Volcanoes of the Southwest Indian Ocean. Active Volcanoes of
781 the World. Springer, Berlin, Heidelberg.
782 Philpotts, A.R., Lewis, C.L., 1987. Pipe vesicles—An alternate model for their origin. Geology
783 15 (10), 971–974.
784 Renggli C.J., Hellmann J.L., Burkhardt C., Klemme S., Berndt J., Pangritz P., Kleine T., 2022.
785 Tellurium isotope fractionation during evaporation from silicate melts, Geochim.
786 Cosmochim. Acta 339, 35-45.
787 Rinnert, E., Cathalot, C., Feuillet, N., 2021. GEOFLAMME cruise, RV Pourquoi pas ?,
788 https://doi.org/10.17600/18001297.
789 Rinnert, E., Lebas, E., Paquet, F., Jorry, S., Feuillet, N., Thinon, I., Fouquet, Y., 2019. MAYOBS
790 cruises, https://doi.org/10.18142/291.
791 Rosca C., Vlastélic I., Varas-Reus M.I., König S, 2022. Isotopic constraints on selenium
792 degassing from basaltic magma and near-surface capture by fumarolic deposits:
793 Implications for Se redistribution onto the Earth's surface. Chem. Geol. 596, 120796.

794 Rubin, K., 1997. Degassing of metals and metalloids from erupting seamount and mid-ocean
795 ridge volcanoes: Observations and predictions. Geochim. Cosmochim. Acta 61, 3525–
796 3542.
797 Shannon R.D., 1976. Revised effective ionic radii and systematic studies of interatomic
798 distances in halides and chalcogenides. Acta Cryst. A32, 751–767.
799 Sharma, V.K., McDonald, T.J., Sohn, M. et al., 2015. Biogeochemistry of selenium. A review.
800 Environ. Chem. Lett. 13, 49–58.
801 Smietana, M., Bachèlery, P., Hémond, C. (2010) Heterogeneity in the mantle source of La
802 Réunion Island. In: Geochim. Cosmochim. Acta, Goldschmidt conference 2010 abstract
803 74, pp A972.
804 Smietana, M., 2011. Pétrologie, géochronologie (K–Ar) et géochimie élémentaire et
805 isotopique (Sr, Nd, Hf, Pb) de laves anciennes de la Réunion: Implications sur la
806 construction de l'édifice volcanique. PhD thesis, Université de la Réunion.
807 Thinon, I., Lemoine, A., Leroy, S., Paquet, F., Berthod, C., Zaragosi, S., Famin, V., Feuillet, N.,
808 Boymond, P., Masquelet, C., Mercury, N., Rusquet, A., Scalabrin, C., Van der Woerd, J.,
809 Bernard, J., Bignon, J., Clouard, V., Doubre, C., Jacques, E., Jorry, S.J., Rolandone, F.,
810 Chamot-Rooke, N., Delescluse, M., Franke, D., Watremez, L., Bachèlery, P., Michon, L.,
811 Sauter, D., Bujan, S., Canva, A., Dassie, E., Roche, V., Ali, S., Sitti Allaouia, A.H., Deplus,
812 C., Rad, S., Sadeski, L., 2022. Volcanism and tectonics unveiled in the Comoros
813 Archipelago between Africa and Madagascar. Comptes Rendus Géoscience 354, 1–28.
814 Upton, B.G.J., Wadsworth, W. J., 1972. Aspects of magmatic evolution on Réunion Island.
815 Philosophical Transactions of the Royal Society of London, Series A 271, 105–130.
816 Upton B.G.J., Semet M.P., Joron J.-L., 2000. Cumulate clasts in the Bellecombe Ash Member,
817 Piton de la Fournaise, Reunion Island, and their bearing on cumulative processes in the
818 petrogenesis of the Réunion lavas. J. Volcanol. Geotherm. Res. 104, 297–318.
819 Verdurme et al., 2024. Magma ascent and lava flow field emplacement during the 2018–2021
820 Fani Maoré deep-submarine eruption insights from lava vesicle textures. Earth Planet.
821 Sci. Lett. 636, 118720.
822 Villemant, B., Salaün, A., Staudacher, T., 2009. Evidence for a homogeneous primary magma
823 at Piton de la Fournaise (La Réunion): A geochemical study of matrix glass, melt
824 inclusions and Pélé's hairs of the 1998–2008 eruptive activity. J. Volcanol. Geotherm.
825 Res. 184, 79–92.

826 Vigouroux, N., Williams-Jones, A. E., Wallace, P., Staudacher, T., 2009. The November 2002
827 eruption of Piton de la Fournaise, Réunion: tracking the pre-eruptive thermal evolution
828 of magma using melt inclusions. Bull. Volcanol. 71, 1077-1089.
829 Vlastélic I., Lewin, E., Staudacher, T., 2006. Th/U and other geochemical evidence for the
830 Reunion plume sampling a less differentiated mantle domain. Earth Planet. Sci. Lett.
831 248, 364-378.
832 Vlastélic, I., Ménard, G., Gannoun, A., Piro, J.-L., Staudacher, T., Famin, V., 2013. Magma
833 degassing during the April 2007 collapse of Piton de la Fournaise: the record of semi-
834 volatile trace elements (Li, B, Cu, In, Sn, Cd, Re, Tl, Bi). J. Volcanol. Geotherm. Res. 254,
835 94–107.
836 Vlastélic, I., Di Muro, A., Bachèlery, P., Gurioli, L., Gannoun, A., Auclair, D. (2018) Control of
837 source fertility on the eruptive activity of Piton de la Fournaise volcano, La Réunion.
838 Sci. Rep. 8, 14478.
839 Vlastélic, I., Piro, J.-L., 2022. Volatilization of trace elements during evaporation to dryness of
840 HF-dissolved silicates (BHVO-2, AGV-1, BIR-1, UB-N): Open versus closed system
841 conditions. Geostand. Geoanal. Res. 46, 519-534.
842 Wang, Z., Becker, H., 2013. Ratios of S, Se and Te in the silicate Earth require a volatile-rich
843 late veneer. Nature 499, 328–331.
844 Wykes, J.L., O'Neill, H.S.C., Mavrogenes, J.A., 2015. The Effect of FeO on the Sulfur Content at
845 Sulfide Saturation (SCSS) and the Selenium Content at Selenide Saturation of Silicate
846 Melts. J. Petrol. 56, 1407–1424.
847 Yi, W., Halliday, A. N., Alt, J.C., Lee, D.-C., Rehkämper, M., Garcia, M.O., Langmuir, C.H., Su, Y.,
848 2000. Cadmium, indium, tin, tellurium, and sulfur in oceanic basalts: implications for
849 chalcophile element fractionation in the Earth. J. Geophys. Res. 105(B8), 18927-18948.
850 Yierpan, A., König, S., Labidi, J., Kurzawa, T., Babechuk, M. G., Schoenberg, R., 2018. Chemical
851 sample processing for combined selenium isotope and selenium- tellurium elemental
852 investigation of the Earth's igneous reservoirs. Geochem. Geophys, Geosyst. 19, 516–
853 533.
854 Yierpan, A., König, S., Labidi, J., Schoenberg, R., 2019. Selenium isotope and S-Se-Te elemental
855 systematics along the Pacific-Antarctic ridge: Role of mantle processes. Geochim.
856 Cosmochim. Acta 249, 199–224.

857 Yierpan, A., Redlinger, J., König, S., 2021. Selenium and tellurium in Reykjanes Ridge and
858 Icelandic basalts: evidence for degassing-induced Se isotope fractionation. Geochim.
859 Cosmochim. Acta 313, 155–172.
860 Zelenski, M., Simakin, A., Taran, Y., Kamenetsky, V.S., Malik, N., 2021. Partitioning of elements
861 between high-temperature, low-density aqueous fluid and silicate melt as derived
862 from volcanic gas geochemistry. Geochim. Cosmochim. Acta 295, 112–134.

Table 1: Samples type and location

Site	Volcano	Sample	Composition	Sample type	Location / eruption phase	Lat. °S	Long. °E	Elevation (m)
Reunion	PdN subaerial	CB2150914	Wehrlite	Cumulate	LM	-21.07	55.50	876
		SAL 206	Wehrlite	Cumulate	Phase I	-21.08	55.50	1077
		BSUZ 2	SSB	Lava flow	Phase I	-21.00	55.42	500
		SAL 51	SSB	Dyke in breccia	Phase I	-21.06	55.49	830
		SAL 48	SSB	Dyke in breccia	Phase I	-21.06	55.49	830
		RUN 008-2006	Hawaiite	Lava flow	Phase III	-21.12	55.27	220
		RUN 038-2006	Benmoreite	Lava flow	Phase IV	-21.09	55.55	1505
		RUN 048-2006	Benmoreite	Lava flow	Phase IV	-21.07	55.38	2020
		SAB 1	Trachyte	Dyke	Phase IV	-21.07	55.47	1710
		SAL 88	Trachyte	Sill in breccia	Phase IV	-21.06	55.51	858
		SAL 200	Trachyte	Sill in breccia	Phase IV	-21.07	55.50	820
		SAL 203	Trachyte*	Sill in breccia	Phase IV	-21.06	55.49	880
		SAL 201	Trachyte*	Sill in breccia	Phase IV	-21.07	55.50	890
	PdF subaerial	CHI-7	Wehrlite	Peridotite	Piton Chisny	-21.24	55.67	2363
		REU 070402-1b	SSB	Lava flow	April 2007 eruption	-21.28	55.77	580
		REU 070403-b	SSB	Lava flow	April 2007 eruption	-21.28	55.77	580
		REU 070404-b	SSB	Lava flow	April 2007 eruption	-21.28	55.77	580
		REU 070408-1b	Olivine-rich basalt	Lava flow	April 2007 eruption	-21.28	55.77	580
		REU 150731-7	SSB	Golden pumice	July 2015 eruption	-21.22	55.71	2139
		REU 180413-1	SSB	Lava crust	April 2018 eruption	-21.21	55.72	1920
		REU 180403	SSB	Scoria	April 2018 eruption	-21.21	55.72	1920
		REU 180713-1	SSB	Lava, water quenched	July 2018 eruption	-21.23	55.70	2230
		REU 200409-6	SSB	Pele hairs	April 2020 eruption	-21.23	55.66	2269
	PdN submarine	ERO2 DR6-2	SSB	Pillow lava	Etang Salé Ridge, 2.48 Ma	-21.35	55.24	-2000
		ERO2 DR7-4B	SSB	Pillow lava	Etang Salé Ridge	-21.35	55.24	-1780
		ERO2 DR7-3	SSB	Pillow lava	Etang Salé Ridge	-21.35	55.24	-1780
		ERO2 DR7-5	SSB	Pillow lava	Etang Salé Ridge	-21.35	55.24	-1780
	PdF submarine	ERO2 DR2-6	SSB	Pillow lava	North of PdF NE Rift Zone, 3.34 Ma	-21.09	55.86	-1700
		GSR2-DR11-47	Mg-rich basalt	Pillow lava	North of PdF NE Rift Zone, 3.77 Ma	-21.09	55.86	-1850
		ERO2 DR8-7	Mg-rich basalt	Pillow lava	South of PdF NE Rift Zone, 0.439 Ma	-21.20	55.91	-1443
		ERO2 DR8-1	Mg-rich basalt	Pillow lava	South of PdF NE Rift Zone, 0.439 Ma	-21.20	55.91	-1443
		ERO2 DR8-6	Mg-rich basalt	Pillow lava	South of PdF NE Rift Zone, 0.439 Ma	-21.20	55.91	-1443
		ERO2 DR8-8	Mg-rich basalt	Pillow lava	South of PdF NE Rift Zone, 0.439 Ma	-21.20	55.91	-1443
Mayotte	Fani Maoré	MAY01-DR01-05	Evolved basanite	Pillow lava	Phase 1 (July 2018 - May 2019)	-12.91	45.72	-2935
		MAY02-DR08-01ALF	Evolved basanite	Pillow lava	Phase 2 (May 2019 - August 2019)	-12.94	45.71	-3061
		MAY02-DR08-0102MB	Evolved basanite	Pillow lava	Phase 2 (May 2019 - August 2019)	-12.94	45.71	-3061
		MAY04-DR10-07	Evolved basanite	Pillow lava	Phase 1 (July 2018 - May 2019)	-12.92	45.72	-3035
		MAY04-DR11-0704-2	Evolved basanite	Pillow lava	Phase 2 (May 2019 - August 2019)	-12.92	45.69	-3239
		MAY04-DR12-0301	Evolved basanite	Pillow lava	Phase 1 (July 2018 - May 2019)	-12.88	45.72	-3222
		MAY04-DR11-0704	Evolved basanite	Pillow lava	Phase 2 (May 2019 - August 2019)	-12.92	45.69	-3239
		GFL-DR20-0101	Evolved basanite	Pillow lava	Phase 3b (October 2020 - January 2021)	-12.87	45.67	-3179

SSB : Steady State Basalts. Most common basalts at La Réunion Island, with composition transitionnal between tholeiites and alkali basalts

PdN : Piton des Neiges. PdF : Piton de la Fournaise.

* With hydrothermal pyrite

Table 2: S, Se and Te concentrations of La Réunion and Mayotte samples

Site	Volcano	Sample		MgO (wt%)	[S] ppm	SD		[Se] ppb	SD		[Te] ppb	SD	
		BHVO-2			185	± 7	(n=10)	170	± 11	(n=20)	14.52	± 0.77	(n=14)
		BCR-2			341	± 1	(n=2)	79.6	± 0.8	(r=3)	2.84	± 0.07	(r=3)
		BE-N			336	± 5	(r=1)	71.7	± 0.9	(r=1)	1.06	± 0.01	(r=2)
		BIR-1			4.43	± 0.04	(r=3)	16.1	± 0.04	(r=2)	5.90	± 0.06	(r=1)
La Réunion	PdN subaerial	CB2150914		33.0	358	± 1.9		35.9	± 1.2		2.72	± 0.04	
		SAL 206		41.5	264	± 2.8		18.9	± 0.6		3.11	± 0.05	
		BSUZ 2		6.5	30	± 0.2		71.0	± 2.4		0.38	± 0.02	
		SAL 51		6.7	257	± 2.5		132	± 4.2		8.76	± 0.07	
		SAL 48		8.2	141	± 1.1		93.4	± 3.3		2.95	± 0.04	
		RUN 008-2006		4.4	28	± 0.3		37.9	± 1.3		0.25	± 0.02	
		RUN 038-2006		1.4	10	± 0.2		3.0	± 0.2		0.46	± 0.02	
		RUN 048-2006		2.4	40	± 0.3		11.6	± 0.4		1.00	± 0.03	
		SAB 1		0.4	4.9	± 0.1		2.0	± 0.2		0.27	± 0.01	
		SAL 88		0.6	-			0.7	± 0.1		0.19	± 0.02	
		SAL 200		2.3	168	± 1.2		23.0	± 0.9		0.64	± 0.03	
		SAL 203		2.8	730	± 5.4		75.8	± 2.5		1.30	± 0.02	
		SAL 201		4.4	884	± 11		206	± 5.0		2.47	± 0.03	
	PdF subaerial	CHI-7		33.4	13	± 0.1		10.0	± 0.4		2.56	± 0.12	
		070402-1b		7.3	101	± 1.6		124	± 2.7		2.16	± 0.21	
		070403-b		7.5	266	± 1.8		130	± 2.9		1.54	± 0.15	
		070404-b		7.3	102	± 1.2		134	± 2.7		1.07	± 0.11	
		070408-1b		29.2	24	± 0.3		59.3	± 1.0		0.69	± 0.09	
		150731-7		6.4	245	± 3.1		131	± 2.7		0.74	± 0.01	
		180413-1		6.9	199	± 2.5		134	± 2.9		0.87	± 0.09	
		180403		6.9	210	± 2.8		133	± 2.2		1.53	± 0.17	
		180713-1		6.9	147	± 0.6		127	± 2.7		0.56	± 0.05	
		200409-6		8.0	196	± 0.8		677	± 10		120	± 6	
	PdN submarine	DR6-2		7.6	416	± 1.7		96.7	± 2.4		3.73	± 0.23	
		DR7-4B		5.1	119	± 0.7		51.0	± 2.1		22.8	± 0.79	
		DR7-3		6.2	437	± 4.3		112	± 2.9		61.6	± 4.88	
		DR7-5		5.5	146	± 0.8		33.8	± 1.1		33.0	± 0.63	
	PdF submarine	DR2-6		6.7	165	± 1.0		74.3	± 1.8		9.54	± 0.52	
		GSR2-DR11-47		10.5	564	± 3.0		116	± 5.4		4.47	± 0.21	
		DR8-7		10.9	632	± 7.5		125	± 2.6		6.95	± 0.07	
		DR8-1		13.1	551	± 5.8		112	± 2.4		12.4	± 0.55	
		DR8-6		9.6	502	± 4.0		109	± 3.1		3.71	± 0.02	
		DR8-8		12.0	435	± 4.9		89.9	± 1.8		6.04	± 0.26	
Mayotte	Fani Maoré	MAY01-DR01-05		4.77	1342	± 32		76.7	± 1.1		6.15	± 0.06	
		MAY02-DR08-01ALF		3.77	1509	± 40		68.2	± 1.1		9.53	± 0.07	
		MAY02-DR08-0102MB		3.79	1454	± 32		69.4	± 1.0		13.6	± 0.10	
		MAY04-DR10-07		4.18	1413	± 41		72.8	± 1.0		6.26	± 0.05	
		MAY04-DR11-0704-2		3.97	1386	± 32		66.5	± 1.2		4.43	± 0.06	
		MAY04-DR12-0301		4.52	1367	± 39		80.7	± 1.3		5.71	± 0.06	
		MAY04-DR11-0704		9.89	1430	± 25		67.3	± 1.1		5.48	± 0.06	
		GFL-DR20-0101 drilling	Bulk distance to pillow rim	4.45	1711			81.5			5.23		
		DR20-1	21.3 cm		1794	± 30		83.5	± 2.1		4.89	± 0.05	
		DR20-3	17.5 cm		1671	± 26		82.6	± 2.0		4.79	± 0.06	
		DR20-5	13.5 cm		1593	± 47		76.8	± 1.7		4.70	± 0.06	
		DR20-7	9.5 cm		1518	± 37		77.0	± 2.0		4.47	± 0.05	
		DR20-9	5.5 cm		1625	± 34		81.4	± 1.6		4.87	± 0.05	
		DR20-10	3.5 cm		1768	± 49		83.2	± 1.7		5.75	± 0.06	
		DR20-11	2 cm		1751	± 35		82.1	± 1.4		5.94	± 0.06	
		DR20-12	1 cm		1801	± 35		83.6	± 1.6		6.04	± 0.08	
		DR20-SP	0 cm		1881	± 30		83.1	± 1.8		5.65	± 0.07	

n: dissolution & chemistry duplicate

r : analysis replicate (same solution)

SD : sample SD is calculated by propagating errors on isotopic ratios (see text)

MgO data are from the supplementary table S1 (La Reunion) and from Berthod et al. (2022)

PdN : Piton des Neiges. PdF : Piton de la Fournaise.

F1

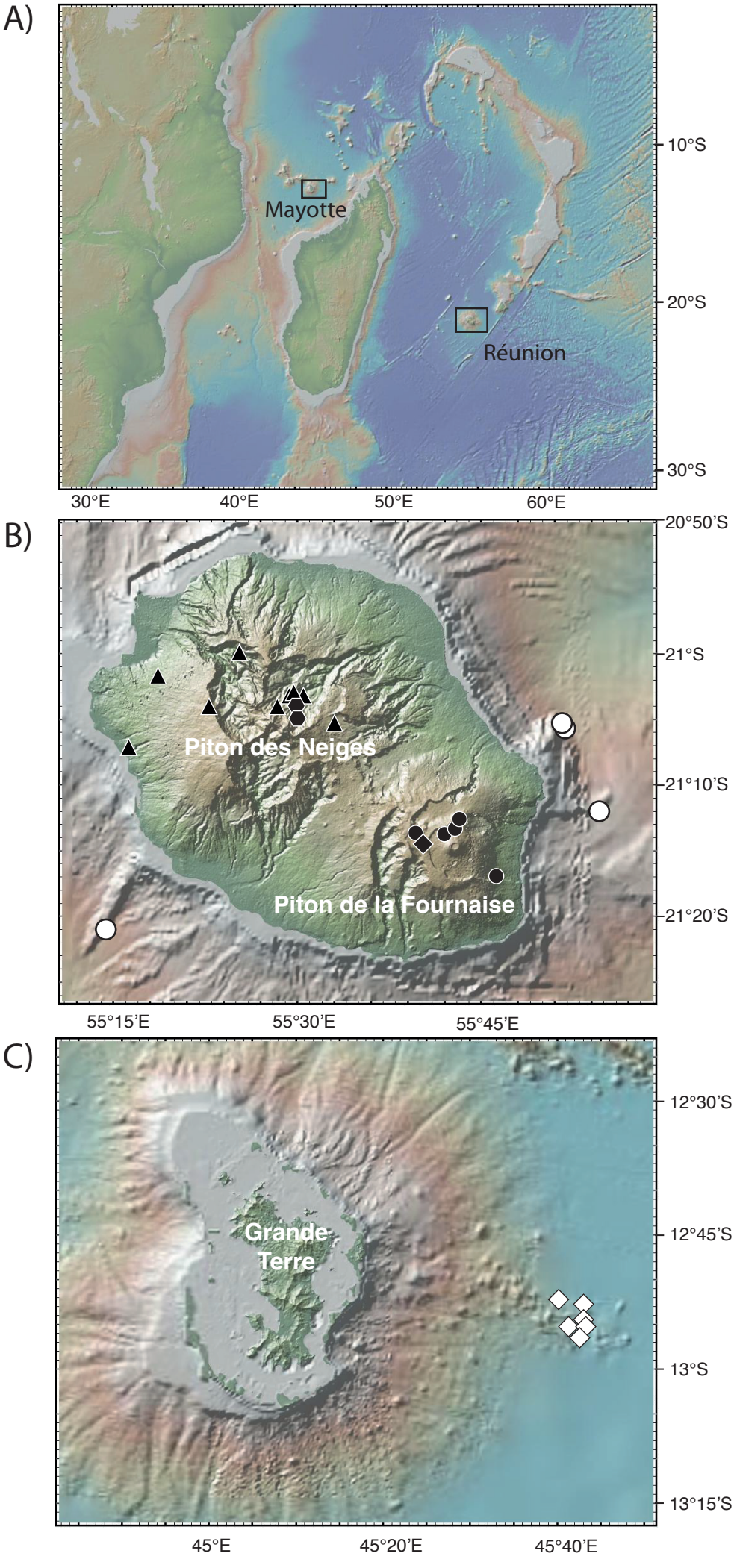
A)
Mayotte
Réunion
10°S
20°S
30°S
30°E
40°E
50°E
60°E
B)
Piton des Neiges
Piton de la Fournaise
20°50'S
21°S
21°10'S
21°20'S
55°15'E
55°30'E
55°45'E
C)
Grande Terre
12°30'S
12°45'S
13°S
13°15'S
45°E
45°20'E
45°40'E

F2

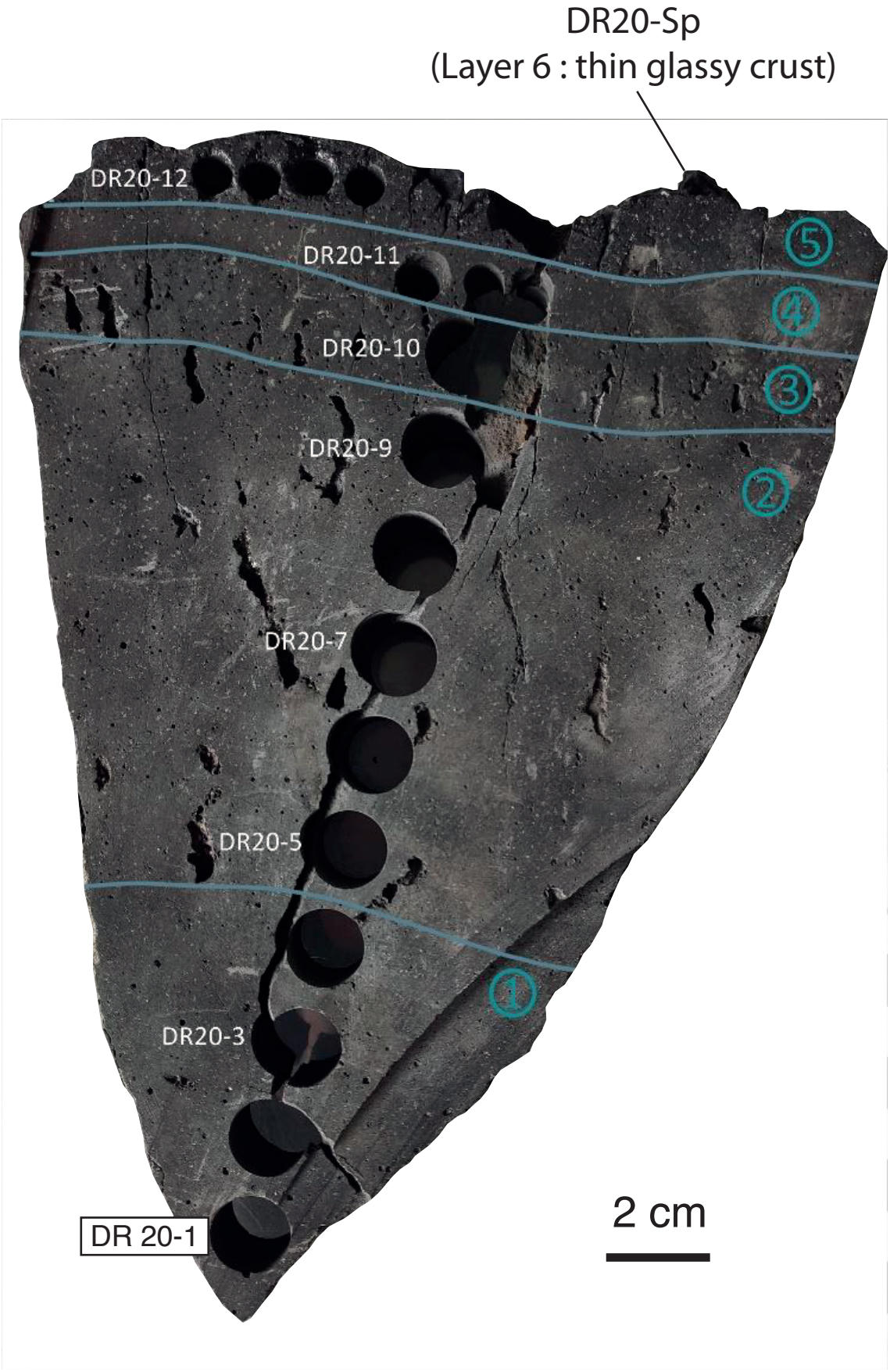
DR20-Sp
(Layer 6 : thin glassy crust)
DR20-12
DR20-11
DR20-10
DR20-9
DR20-7
DR20-5
DR20-3
DR 20-1
5
4
3
2
1
2 cm

F3

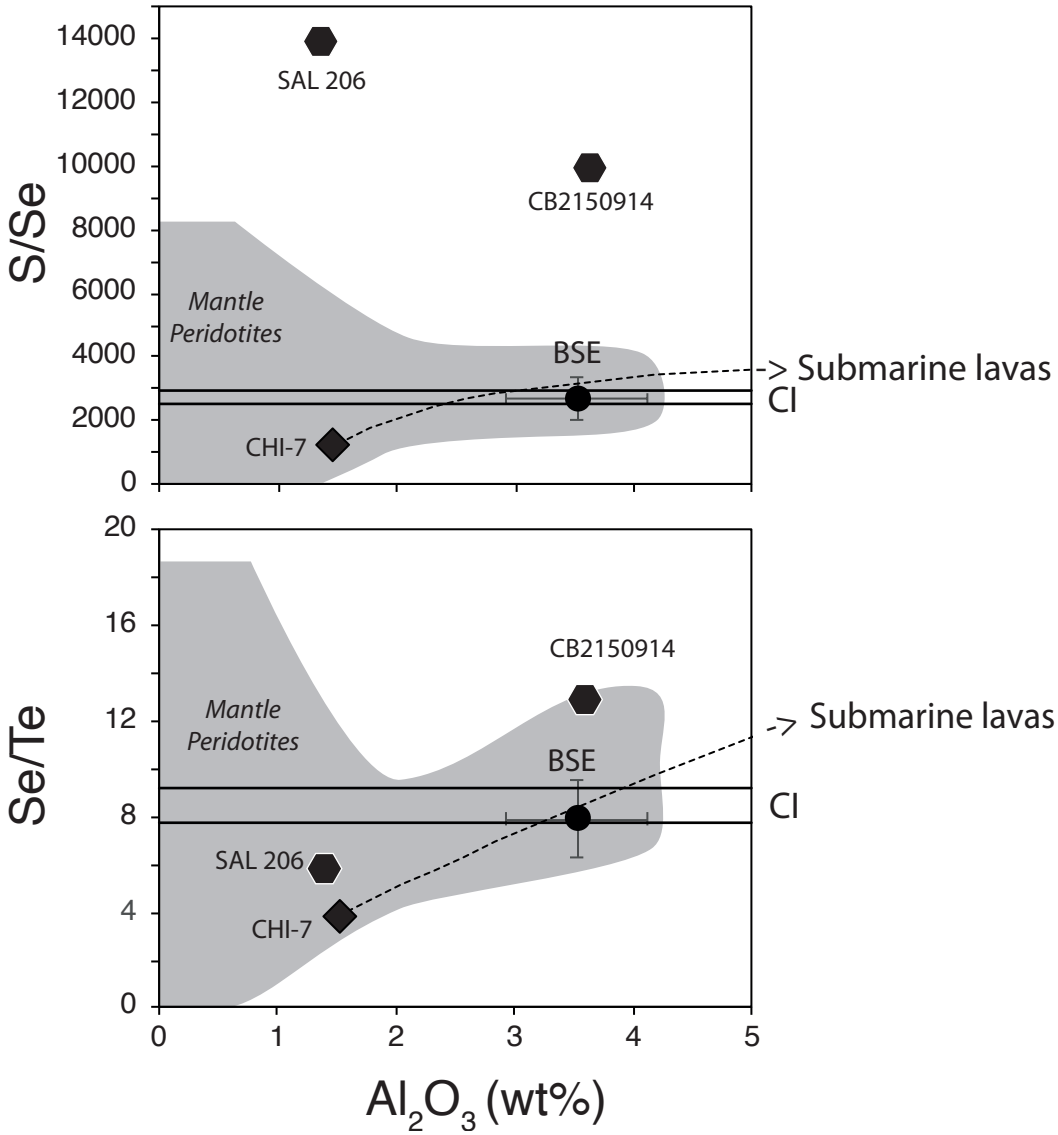
14000
12000
10000
8000
6000
4000
2000
0
S/Se
SAL 206
CB2150914
Mantle
Peridotites
BSE
-> Submarine lavas
CI
CHI-7
20
16
12
8
4
0
Se/Te
CB2150914
Mantle
Peridotites
-> Submarine lavas
BSE
CI
SAL 206
CHI-7
0
1
2
3
4
5
Al2O3 (wt%)

F4

Crystallization assemblage

La Réunion
(1) Ol + Spl
(2) Ol + Cpx + Plg + Spl
(3) Cpx + Plg + Sulf
(4) Cpx + Plg + Mnt + Sulf

Fani Maoré eruption (Mayotte)
(2-3) 80% Cpx + 20% Ol + Sulf

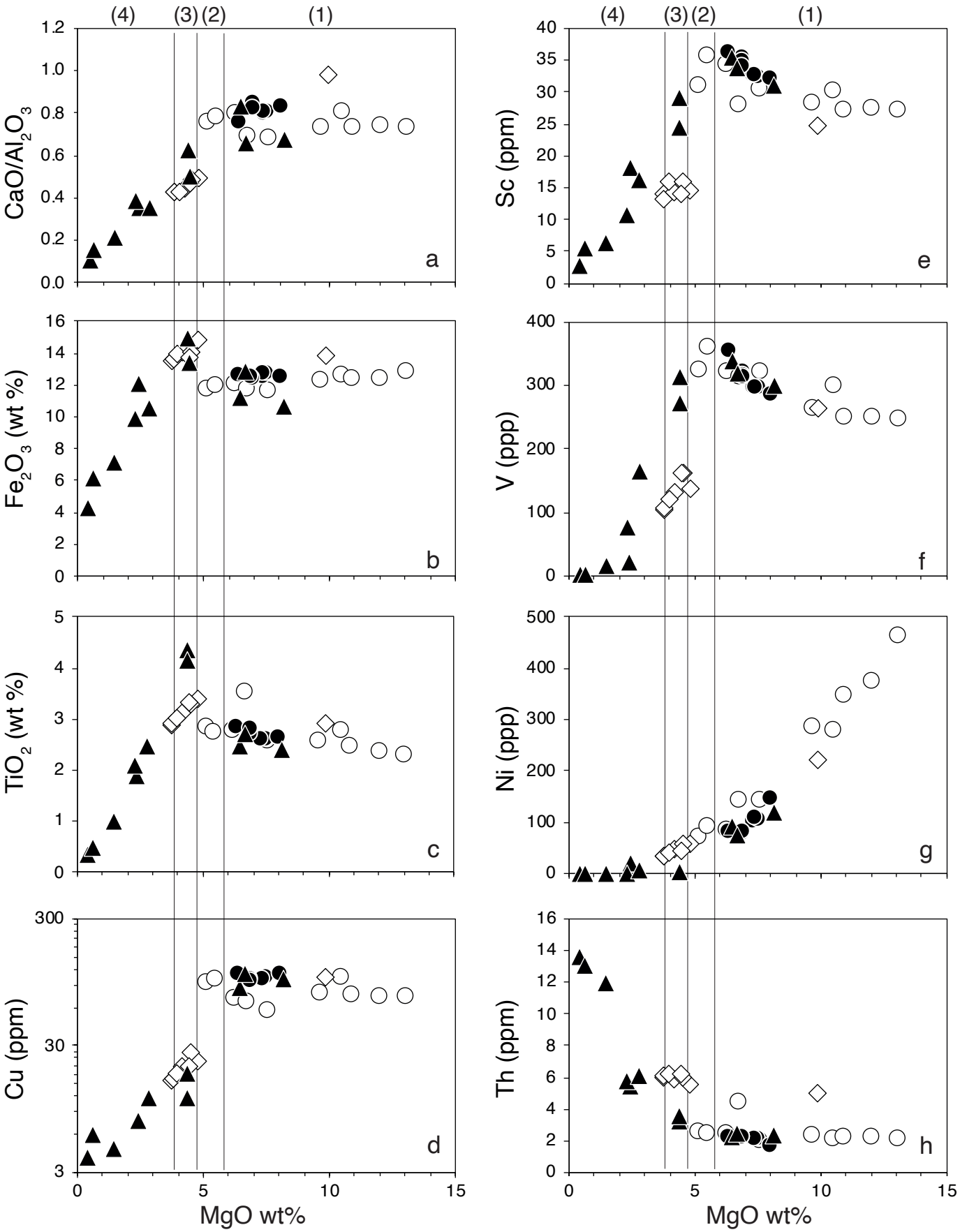

F5

Crystallization assemblage

La Réunion
(1) Ol + Spl
(2) Ol + Cpx + Plg + Spl
(3) Cpx + Plg + Sulf
(4) Cpx + Plg + Mnt + Sulf

Fani Maoré eruption (Mayotte)
(2-3) 80% Cpx + 20% Ol + Sulf

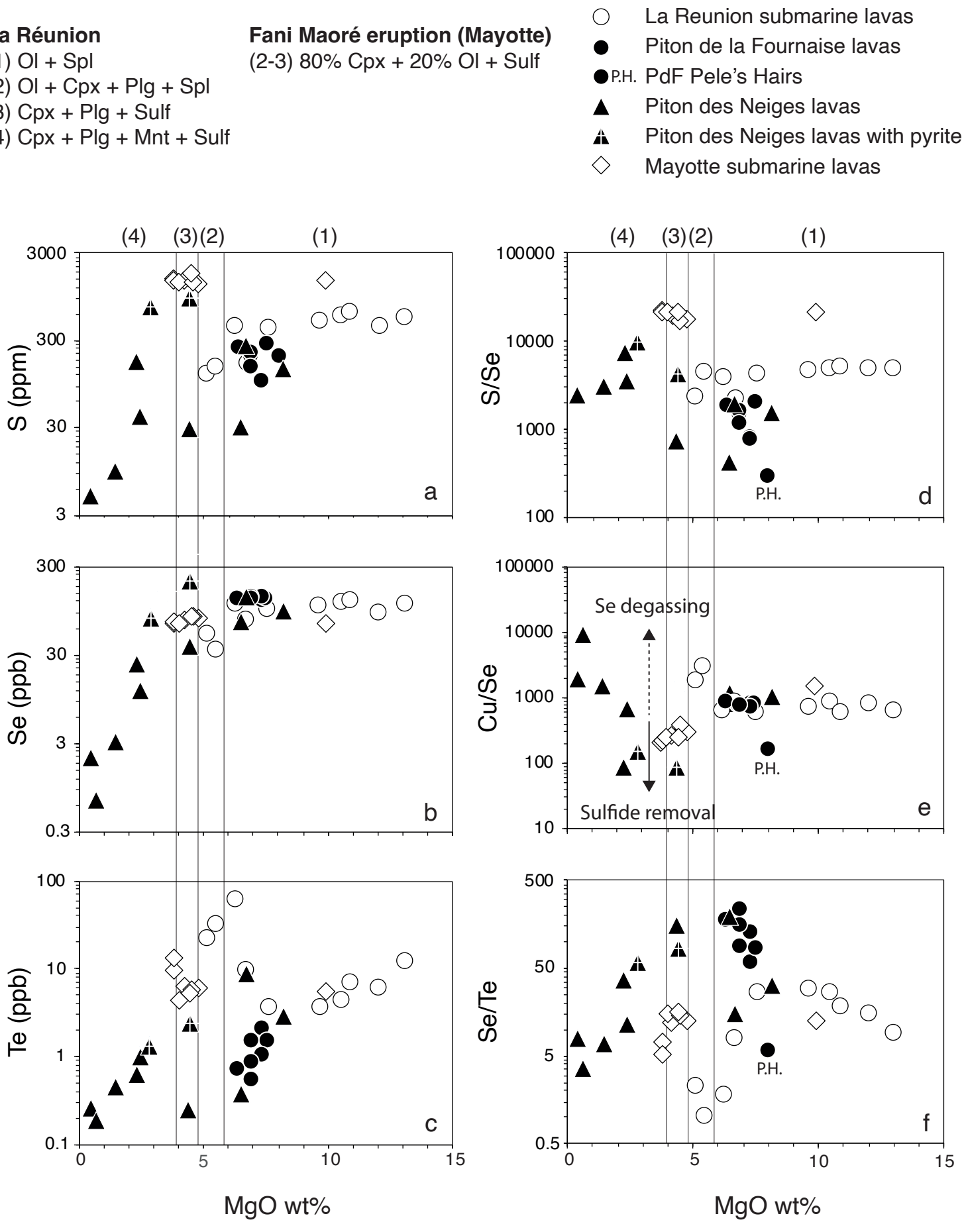

F6

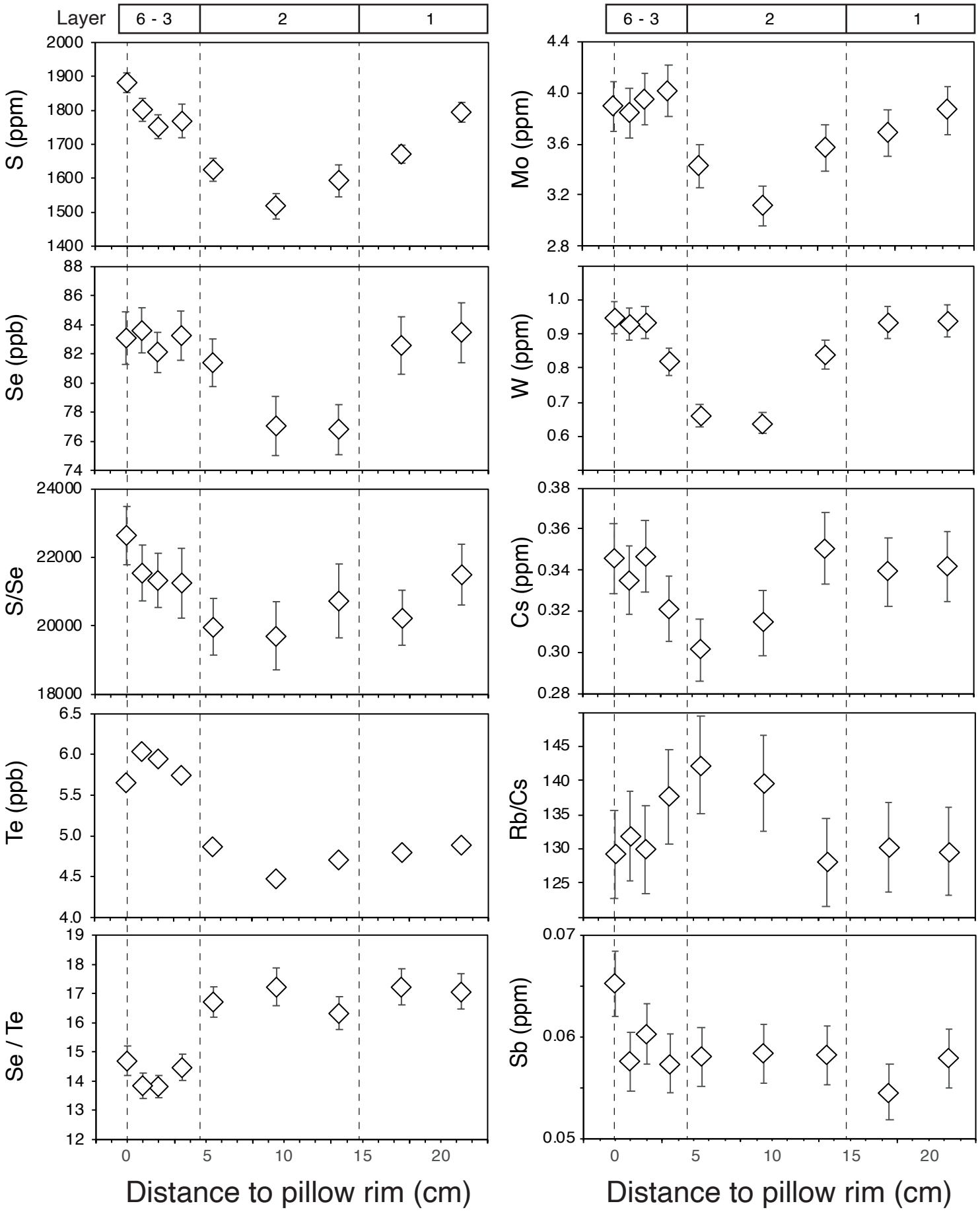
Layer
6 - 3
2
1
S (ppm)
Se (ppb)
S/Se
Te (ppb)
Se / Te
Mo (ppm)
W (ppm)
Cs (ppm)
Rb/Cs
Sb (ppm)
Distance to pillow rim (cm)
Distance to pillow rim (cm)